

1 **The variation and visualisation of elastic anisotropy in rock-forming minerals**

2 David Healy¹, Nicholas E. Timms² & Mark A. Pearce³

3 ¹: School of Geosciences, King's College, University of Aberdeen, Aberdeen AB24 3UE, United
4 Kingdom

5 ²: Space Science and Technology Centre, School of Earth and Planetary Sciences, Curtin
6 University, Perth, GPO Box U1987, WA 6845, Australia

7 ³: CSIRO Mineral Resources, Australian Resources Research Centre, 26 Dick Perry Avenue,
8 Kensington, WA 6151, Australia

9 *corresponding author: d.healy@abdn.ac.uk

10

11 **Abstract**

12 All minerals behave elastically, a rheological property that controls their ability to support stress,
13 strain and pressure, the nature of acoustic wave propagation and influences subsequent plastic (i.e.
14 permanent, non-reversible) deformation. All minerals are intrinsically anisotropic in their elastic
15 properties – that is, they have directional variations that are related to the configuration of the
16 crystal lattice. This means that the commonly used mechanical elastic properties that relate elastic
17 stress to elastic strain, including Young's modulus (E), Poisson's ratio (ν), shear modulus (G) and
18 linear compressibility (β), are dependent on crystallographic direction. In this paper, we explore the
19 ranges of anisotropy of E , ν , G and β in 86 rock-forming minerals, using previously published data,
20 and show that the range is much wider than commonly assumed. We also explore how these
21 variations (the directionality and the magnitude) are important for fundamental processes in the
22 solid earth, including deformation (mechanical) twinning, coherent phase transformations and
23 brittle failure. We present a new open source software package (AnisoVis, written in MATLAB),
24 which we use to calculate and visualise directional variations in elastic properties of rock-forming
25 minerals. Following previous work in the fields of chemistry and materials, we demonstrate that by
26 visualising the variations in elasticity, we discover previously unreported properties of rock-
27 forming minerals. For example, we show previously unreported directions of negative Poisson's
28 ratio and negative linear compressibility and we show that the existence of these features is more
29 widespread (i.e. present in many more minerals) than previously thought. We illustrate the
30 consequences of intrinsic elastic anisotropy for the elastic normal and shear strains within α -quartz
31 single crystal under different applied stress fields; the role of elastic anisotropy on Dauphiné
32 twinning and the α - β phase transformations in quartz; and stress distributions around voids of
33 different shapes in talc, lizardite, albite, and sanidine. In addition to our specific examples, elastic
34 anisotropy in rock-forming minerals to the degree that we describe has significant consequences for
35 seismic (acoustic) anisotropy, the focal mechanisms of earthquakes in anisotropic source regions
36 (e.g. subducting slabs), for a range of brittle and ductile deformation mechanisms in minerals, and
37 geobarometry using mineral inclusions.

38

39

40 **Introduction**

41 The elastic deformation of rock-forming minerals plays an important role in many earth processes.
42 The increased availability of measured or calculated elastic properties of whole rocks and of
43 specific rock-forming minerals has led to advances in many fields of earth science, including
44 seismology, geodynamics, tectonics and metamorphism. Minerals have long been known to display
45 anisotropy – directional variations – in their elastic properties (Mandell, 1927; Birch & Dancroft,
46 1938; Hearmon, 1946), and that these variations show a close relationship to the symmetry of the
47 mineral crystallographic structure (e.g. Angel et al., 2012; Timms et al., 2018). Advances in
48 laboratory methods of measurement (acoustic velocities, Brillouin scattering, resonant ultrasound)
49 and in theoretical techniques for *ab initio* molecular dynamics calculations has allowed scientists to
50 quantify this anisotropy for a wide range of rock-forming minerals. For this paper we have collected
51 246 published datasets (measurements or *ab initio* calculations) of anisotropic elastic properties
52 covering 86 distinct minerals. Elastic anisotropy is fully described by a fourth rank tensor
53 (compliance or stiffness, see below), and published data are commonly presented in a Voigt matrix
54 format, listing up to 21 independent values (depending on the crystal symmetry class), whereas
55 elastically isotropic minerals require only 2 independent values. A key aim of this paper is to use
56 published data to visualise and explore elastic anisotropy in rock-forming minerals using familiar
57 measures, such as Young's modulus and Poisson's ratio, but presented in novel formats and thereby
58 render the increasing volume of data more transparent to analysis. As noted by previous authors
59 (Karki & Chennamsetty, 2006; Lethbridge et al., 2010; Marmier et al., 2010; Gaillac et al., 2016),
60 graphical depictions of the directional variation of elastic properties provide new opportunities to
61 relate the quantitative data to the crystalline structure of the mineral. This in turn allows us to relate
62 the observed or predicted mechanical and chemical behaviour of the mineral to specific
63 crystallographic directions.

64 It has long been recognized that the velocity of seismic waves passing through rocks is a direct
65 function of the minerals' elastic properties and their density, expressed through the Christoffel
66 equation (Christoffel, 1877; Zhou & Greenhalgh, 2004). By considering rocks as polycrystalline
67 aggregates various workers have modelled seismic velocities, and their anisotropy, by combining
68 single mineral elasticity data with different averaging schemes due to Reuss, Voigt or Hill (e.g.
69 Mainprice, 1990; Lloyd & Kendall, 2005). This 'rock recipe' approach has improved our
70 understanding of the composition and structure of the lower crust and mantle and provided useful
71 constraints for alternative models for observed variations in seismic anisotropy beneath continents
72 and around arcs (e.g. Kern, 1982; Tatham et al., 2008; Healy et al., 2009).

73 Inclusions of one mineral or fluid within another host mineral have been used to estimate pressures
74 at the time of inclusion or entrapment (Rosenfeld & Chase, 1961; Rosenfeld, 1969; Chopin, 1984;
75 Gillet et al., 1984; van der Molen & van Roermund, 1986; Angel et al., 2014; Angel et al., 2015).
76 The analysis critically depends on the elastic properties of the host mineral and, in the case of solid
77 inclusions, of the inclusion itself, typically expressed as the bulk and shear moduli (e.g.
78 Mazzucchelli et al., 2018). The underlying theory is based on the classical analysis by Eshelby
79 (1957, 1959) who derived the equations for the deformation within an ellipsoidal inclusion and host
80 due to the imposition of a far-field load. Most of the work to date has simplified the analysis to
81 assume isotropy in both the inclusion and the host, although see Zhang (1998) for a rare exception.
82 Therefore, the full effects of host minerals and inclusion elastic anisotropy on inclusion-based
83 geobarometry have not yet been rigorously investigated. Furthermore, fluid inclusions can

84 decrepitate – i.e. fracture their host and dissipate their fluid – if their internal overpressure rises to a
85 critical value that exceeds the local strength of the enclosing grain. The basis for predicting this
86 behaviour is linear elastic fracture mechanics (LEFM), and the assumption of elastic isotropy is
87 nearly ubiquitous (e.g. Lacazette, 1990).

88 Permanent, non-reversible (i.e. plastic) deformation of minerals is invariably preceded by an elastic
89 response prior to some form of yield condition being reached. For example, the elastic properties of
90 minerals are important in the analysis of brittle cracking at the grain scale. As noted above for the
91 decrepitation of fluid inclusions, the dominant paradigm for this analysis is linear elastic fracture
92 mechanics (LEFM), and the assumption of elastic isotropy. This is important because faults and
93 fractures in rocks are composite structures, built by the interaction and coalescence of many smaller
94 cracks that nucleate at the scale of individual grains i.e. within elastically anisotropic crystals.
95 Jaeger & Cook (1969) used the equations published by Green & Taylor (1939) to consider the
96 stresses developed at the edges of circular holes in anisotropic rocks. In their analysis (repeated in
97 Pollard & Fletcher, 2005), they dismissed the significance of elastic anisotropy because the ratio of
98 maximum to minimum Young's modulus in rocks is 'rarely as high as 2'. Timms et al. (2010)
99 conducted novel indentation experiments in a single crystal of quartz and produced a type of cone
100 fracture with variations in opening angle and crack length that have a trigonal symmetry radiating
101 from the point of contact, and thus demonstrated the key role played by the elastic anisotropy in
102 controlling the fracture geometry. In the same study, these authors confirmed that elastic anisotropy
103 plays a significant role in controlling the focal mechanisms (moment tensors) of acoustic emission
104 events at the scale of a single crystal.

105 Poisson's ratio appears as a term in, for example, the equations describing fracture toughness and
106 indentation, and therefore the precise value of Poisson's ratio is important. Poisson's ratio for
107 isotropic materials is constrained to lie between 0.5 and -1, but there are no theoretical limits for
108 anisotropic materials (Ting & Chen, 2005). Materials with Poisson's ratio less than 0 are termed
109 'auxetic' (Lakes, 1987; Baughman et al., 1998a; Prawoto, 2012; Pasternak & Dyskin, 2012).
110 Fracture toughness and resistance to indentation increase as Poisson's ratio approaches the lower
111 (isotropic) limit of -1.0 (Yeganeh-Haeri et al., 1992). In rock-forming minerals, negative Poisson's
112 ratios have already been documented for α -cristobalite (Yeganeh-Haeri et al., 1992), for quartz at
113 the α - β phase transition (Mainprice & Casey, 1990), for talc (Mainprice et al., 2008), and for calcite
114 and aragonite (Aouni & Wheeler, 2008). A key question therefore is to determine if there are other
115 rock-forming minerals with the same properties, and for which specific crystallographic directions.
116 In a recent review of data on Poisson's ratio in engineering materials, Greaves et al. (2011) pointed
117 out that the brittle-ductile transition at the grain scale is also a function of the elastic properties and
118 therefore likely dependent on direction in strongly anisotropic materials.

119 Elastic properties, and anisotropy, is also known to influence the 'ductile' or plastic deformation of
120 minerals, and has a role in twinning, crystal plasticity (dislocation creep) and phase transformations
121 (e.g. Tullis, 1969; Christian & Mahajan, 1995; Timms et al., 2018). The role of mineral elasticity is
122 also important for inhomogeneous distribution of stresses at the grain scale necessary for driving
123 pressure solution creep, and is either treated implicitly (e.g., Wheeler, 1992) or explicitly (e.g.,
124 Wheeler, 2018). However, in many studies of rock deformation, minerals are commonly assumed to
125 be elastically isotropic and scalar mean values of elastic moduli are used, and/or elastic strains are

126 assumed to be small relative to plastic deformation and so ignored (e.g., in visco-plastic self-
127 consistent (VPSC) code) (Tomé & Lebensohn, 2014).

128 Given the key role that the elastic behavior of minerals plays in so many fundamental geological
129 processes, the scientific need to explore, understand and quantify directional variations in elastic
130 properties in minerals is clear, as is the need to develop better approaches to their graphical
131 visualisation. It is very difficult to full appreciate the variations in elastic properties of a mineral
132 simply by inspection of the 4th rank stiffness (or compliance) tensor, even in reduced form (Voigt
133 notation; see below). A related requirement is the ability to investigate the interactions of mineral
134 elastic anisotropy with imposed pressure, stress, or strain. However, the visualisation and full
135 appreciation of the properties of 2nd rank tensors, such as stress and strain, also presents challenges.
136 No single surface can simultaneously portray the full anisotropy quantified by the diagonal (normal)
137 and off-diagonal (shear) components of these tensorial mechanical quantities. Depictions of strain
138 (or stress) as ellipsoids using only the principal values as semi-axes fail to quantify the directional
139 variations in shear strain (or stress) and cannot easily show examples with mixed positive and
140 negative principal values. We believe there are clear educational benefits to alternative approaches
141 to visualising stress and strain, which students commonly find challenging, both conceptually and
142 from a 3-dimensional cognition perspective. For example, most geological textbooks either
143 illustrate stress or strain as ellipses/ellipsoids of the normal component only (with the limitations
144 described above), Mohr diagrams, or written out in matrix notation. Furthermore, a common
145 misnomer that some minerals are isotropic in material properties undoubtedly stems from the strong
146 emphasis on optical properties of minerals in most undergraduate mineralogy courses. Software
147 tools with the capability of comparative visualisation of various physical properties of minerals in
148 2- and 3-dimensions, including elastic, optical, and acoustic anisotropy have a valuable place in
149 teaching and learning in mineralogy and in scientific research.

150 While the number of published datasets for single mineral elastic anisotropy continues to increase,
151 there are relatively few publications that have reviewed or synthesised the available data. Gercek
152 (2007) provided a useful review of Poisson's ratio for rocks and included some data for specific
153 minerals. A more recent review of Poisson's ratio in rocks (Ji et al., 2018) also contained data for
154 minerals, but used their calculated Voigt-Reuss-Hill average values rather than quantify their
155 anisotropy. Workers in the fields of chemistry, physics and engineering have published methods
156 and tools for visualising the elastic anisotropy of various groups of solid elements and compounds
157 (Karki & Chennamsetty, 2006; Lethbridge et al., 2010; Marmier et al., 2010; Gaillac et al., 2016),
158 and these predominantly focus on Poisson's ratio. In earth sciences, the MTEX toolbox for the
159 analysis and modelling of crystallographic textures from electron backscatter diffraction (EBSD)
160 data provides stereographic projections of elastic properties, such as Young's modulus, for single
161 minerals (Hielscher, R. & Schaeben, H., 2008; Mainprice et al., 2011). The MSAT toolbox for
162 seismic anisotropy also contains options for plotting the elastic anisotropy of rocks and minerals
163 (Walker & Wookey, 2012). Both MTEX and MSAT provide one or more options for displaying the
164 elastic properties of minerals, but their focus is on the analysis of textures and seismic (acoustic)
165 velocity anisotropy, respectively.

166 In this paper, we seek to quantify and visualize the variations in elastic properties of rock-forming
167 minerals. In addition, we present the AnisoVis toolbox, a collection of new MATLAB scripts based
168 on published methods with a graphical user interface (GUI), to explore the range of elastic
169 anisotropy displayed by rock-forming minerals. Specifically, AnisoVis depicts the magnitude of the

170 directional variations in elastic properties such as Young's modulus (E), Poisson's ratio (ν), shear
 171 modulus (G) and linear compressibility (β) using a range of 2- and 3-dimensional representations of
 172 each elastic property to enable a complete assessment of the anisotropy in relation to the crystal
 173 symmetry. We exploit the large database of published elastic constants for rock-forming minerals to
 174 systematically assess the anisotropy of different elastic properties as a function of temperature and
 175 pressure (where possible), giving new insights into the elastic behaviour of rock-forming minerals.
 176 Most of the figures presented in this paper have been produced from the AnisoVis toolbox, which is
 177 freely available on the web.

178 A table of symbols and terms used in this paper is provided in Table 1. Elastic properties are
 179 reported in SI units. In Section 2 we review the theoretical basis of linear elasticity and the formal
 180 description of elastic anisotropy in terms of the key equations. We then describe the methods we
 181 use to visualise and quantify the directional variations in elastic properties for any given mineral.
 182 We present two sets of results. Firstly, we analyse general trends in the database of 86 distinct
 183 minerals with 246 separate elasticity datasets from published sources, and summarise the degree of
 184 anisotropy to be found in rock-forming minerals. Secondly, we analyse specific examples and focus
 185 on their response to applied deformation. We review the key issues raised by these analyses in the
 186 Summary. The Appendix contains benchmarks of the calculations performed in AnisoVis in
 187 comparison to published output from previous workers.

Quantity	Symbol	Default SI unit
Young's modulus	E	Pa
Poisson's ratio	ν	
Shear modulus	G	Pa
Linear compressibility	β	Pa ⁻¹
Bulk modulus	K	Pa
Compliance	s	Pa ⁻¹
Stiffness	c	Pa
Stress	σ	Pa
Strain	ε	
Normal stress	σ_n	Pa
Shear stress	τ	Pa
Normal strain	ε_n	
Shear strain	γ	
Unit vectors parallel to crystallographic axes	$\mathbf{a}, \mathbf{b}, \mathbf{c}$	Miller notation

188 **Table 1.** List of symbols and terms used in this paper, together with their default units (if any).

189

190 **2. Theory and underlying equations**

191 The elastic anisotropy of a solid material is described by a fourth rank tensor, either the compliance
192 s_{ijkl} or its inverse, the stiffness c_{ijkl} (Nye, 1985). For linear elastic deformation, the generalised form
193 of Hooke's Law can be written as:

$$194 \quad \varepsilon_{ij} = s_{ijkl} \sigma_{kl} \quad (1)$$

195 where ε_{ij} and σ_{ij} are the second rank tensors of strain and stress, respectively. Alternatively,
196 equation (1) can be written as:

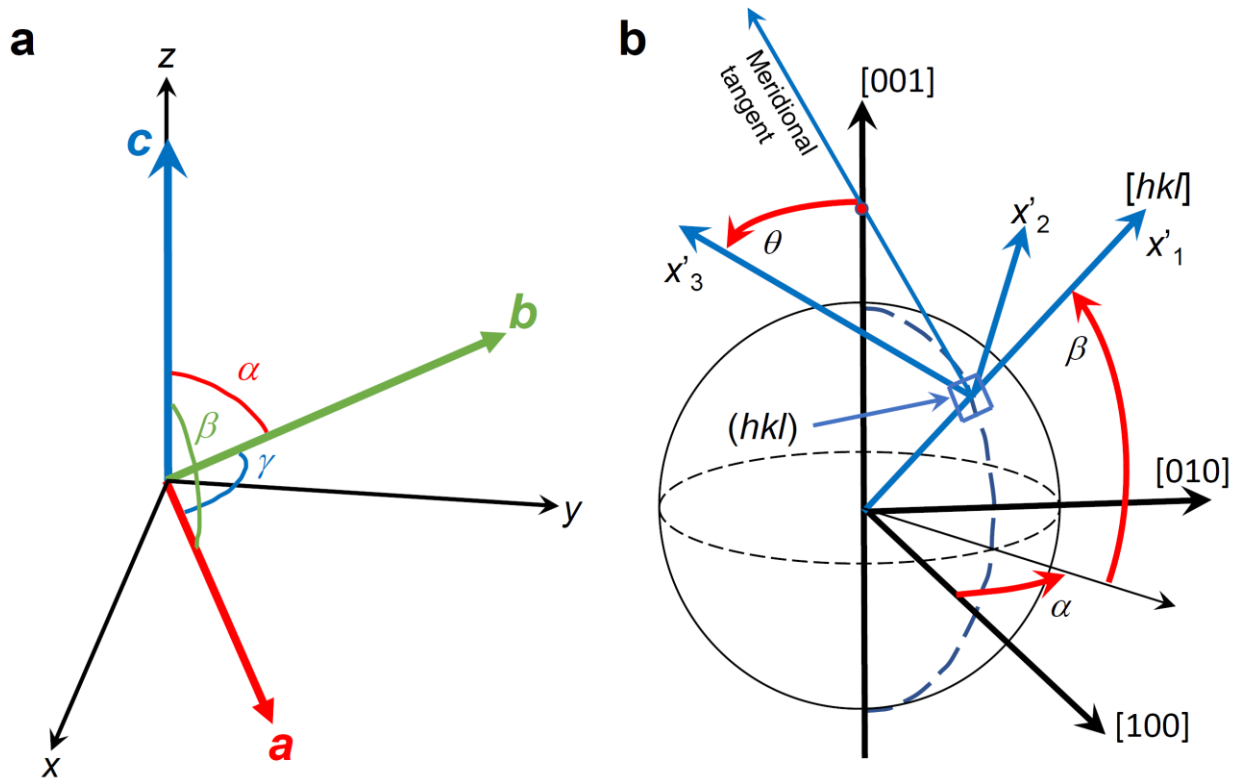
$$197 \quad \sigma_{ij} = c_{ijkl} \varepsilon_{kl} \quad (2).$$

198 Symmetry considerations lead to $s_{ijkl} = s_{ijlk}$ and $s_{ijkl} = s_{jikl}$ (Nye, 1985). The corollary of these
199 relationships is that the number of independent (potentially unique) components of s_{ijkl} is reduced
200 from 81 ($=3^4$) to 36. The same applies to c_{ijkl} . The elastic compliance s or stiffness c of a crystal can
201 therefore be represented in a more compact form, known as the Voigt matrix. This is a square 6 x 6
202 matrix where, for example, the elements of elastic stiffness are defined as $c_{IJ} = c_{ijkl}$, where $I = ij$ and
203 $J = kl$. There are six different permutations of $I(J) = ij(kl)$, the details of which are listed in Nye
204 (1985) and more recently in Almqvist & Mainprice (2017).

205 The measured and calculated elastic properties of single crystals are reported in Voigt matrix
206 notation (s_{IJ} , c_{IJ}), where the indices I, J ($=1,2,3$) relate to a standard Cartesian reference frame ($x=1$,
207 $y=2$, $z=3$). The relationship between any specific crystal lattice and this Cartesian reference is
208 arbitrary, but we adopt the convention described in Britton et al. (2016). In this system:

- 209 • the unit cell lattice vectors \mathbf{a} , \mathbf{b} , and \mathbf{c} form a right-handed set,
- 210 • \mathbf{c} is parallel to Cartesian z ,
- 211 • \mathbf{b} lies in the Cartesian y - z plane at angle α to \mathbf{c} , and
- 212 • \mathbf{a} is directed at angle β to \mathbf{c} and γ to \mathbf{b} .

213 Note that α is the angle between \mathbf{b} and \mathbf{c} , β is the angle between \mathbf{c} and \mathbf{a} and γ is the angle between
214 \mathbf{a} and \mathbf{b} (see Figure 1a).



215

216 **Figure 1. a)** Crystallographic orientation convention (after Britton et al., 2016) and **b)** geometrical
 217 reference frame (after Turley & Sines, 1971) used in this paper.

218 Familiar elastic properties, such as Young's modulus (E), Poisson's ratio (ν) and shear modulus
 219 (G), can be expressed directly in terms of the components of the compliance matrix. For example,
 220 the Young's modulus of a single crystal for a uniaxial stress applied in the x -direction is:

221
$$E_x = E_l = 1 / s_{11} \quad (3)$$

222 and the Poisson's ratio for a uniaxial stress and axial strain along x and a lateral strain along y is

223
$$\nu_{xy} = -s_{21} / s_{11} \quad (4)$$

224 Note that, in general for anisotropic materials, $\nu_{xy} \neq \nu_{yx}$ etc.

225 Guo & Wheeler (2006) note that although Poisson's ratio may be negative for some directions,
 226 these are often compensated by higher positive values in transverse directions perpendicular the
 227 minima in the same plane. They suggest a more useful measure of extreme auxeticity, the **areal**
 228 **Poisson's ratio**, defined as the average of all values of Poisson's ratio taken within the plane
 229 normal to a chosen direction. If the areal Poisson's ratio is negative this implies that a cylinder of
 230 the mineral would contract under a uniaxial compression, around the whole circumference, and not
 231 just along certain directions.

232 In order to calculate specific values of these elastic properties in more general directions within a
 233 crystal – i.e. not just along the axes of the default Cartesian reference frame – we need to transform
 234 the compliance matrix into a different reference frame. We follow the notation used by Turley &
 235 Sines (1971) based on Eulerian angles α , β and θ (see Figure 1b) that define the new Cartesian axes

236 (1', 2', 3' or x', y', z') in relation to the initial reference frame (1,2,3 or x, y, z). The transformation
 237 of compliance matrix s_{ijkl} to s'_{ijkl} is given by (Nye, 1985):

$$238 \quad s'_{ijkl} = a_{im} a_{jn} a_{ko} a_{lp} s_{mnop} \quad (5)$$

239 where the elements of the rotation matrix a are given by:

$$240 \quad a_{ij} = \begin{bmatrix} A & B & C \\ (D \sin \theta + E \cos \theta) & (F \sin \theta + G \cos \theta) & H \sin \theta \\ (D \cos \theta - E \sin \theta) & (F \cos \theta - G \sin \theta) & H \cos \theta \end{bmatrix} \quad (6)$$

241 where $A = \cos \alpha \cos \beta$, $B = \sin \alpha \cos \beta$, $C = \sin \beta$, $D = -\cos \alpha \sin \beta$, $E = -\sin \alpha$, $F =$
 242 $-\sin \alpha \sin \beta$, $G = \cos \alpha$, $H = \cos \beta$ (Turley & Sines, 1971).

243 Using the transformed compliance matrix s'_{ijkl} , we can now calculate the elastic properties for any
 244 general direction within the crystal defined by a unit vector with angles α , β and θ , for example:

$$245 \quad E'_1 = 1 / s'_{11} \quad (7)$$

$$246 \quad G'_{12} = 1 / s'_{66} \quad (8)$$

$$247 \quad \nu'_{12} = -s'_{21} / s'_{11} \quad (9)$$

248 To calculate the variation in any elastic property over all possible directions in 3D, we simply need
 249 to vary α and β over a unit sphere (α : 0-360°, β : 0-180°) and vary θ over a unit circle (θ : 0-360°).

250 *Isotropic approximations of anisotropic elastic properties*

251 Two useful 'averaging' schemes that can be applied to the full set of anisotropic elastic properties
 252 of polycrystals are those due to Reuss and Voigt (see Hill, 1952). The bulk and shear moduli in the
 253 Voigt scheme are defined as:

$$254 \quad K^V = [(c_{11} + c_{22} + c_{33}) + 2(c_{12} + c_{23} + c_{31})]/9 \quad (10)$$

$$255 \quad G^V = [(c_{11} + c_{22} + c_{33}) - (c_{12} + c_{23} + c_{31}) + 3(c_{44} + c_{55} + c_{66})]/15 \quad (11)$$

256 and in the Reuss scheme as:

$$257 \quad K^R = 1/[(s_{11} + s_{22} + s_{33}) + 2(s_{12} + s_{23} + s_{31})] \quad (12)$$

$$258 \quad G^R = 15/[4(s_{11} + s_{22} + s_{33}) - 4(s_{12} + s_{23} + s_{31}) + 3(s_{44} + s_{55} + s_{66})] \quad (13)$$

259 The Voigt average of any property always exceeds the Reuss average and the 'true' value lies
 260 somewhere in between. The Voigt-Reuss-Hill (VRH) average of a property is defined as the
 261 arithmetic mean of the Voigt and Reuss estimates e.g. $G^{VRH} = (G^V + G^R)/2$. Note that, although only
 262 formally defined for polycrystals and based on averaging over many grains, the Voigt, Reuss and
 263 VRH estimates are in practice useful for single crystals: if we consider a polycrystal made of many
 264 grains all aligned perfectly parallel, then the elastic anisotropy of this polycrystal is identical to that
 265 of the single crystal.

266 To plot the variations of disparate elastic properties across minerals with widely different
267 symmetries and anisotropies, we use the Universal Anisotropy Index (A^U), of Ranganathan &
268 Ostoja-Starzewski (2008), defined as:

$$269 \quad A^U = 5 \frac{G^V}{G^R} + \frac{K^V}{K^R} - 6 \quad (14)$$

270 where G^V and K^V are the Voigt average shear and bulk moduli, respectively; and G^R and K^R are the
271 Reuss average shear and bulk moduli, respectively. In contrast to previous measures, the Universal
272 Anisotropy Index was designed to incorporate contributions from the bulk part of the elasticity
273 (terms in K) and is unique for a given mineral elasticity (Ranganathan & Ostoja-Starzewski, 2008).
274 A^U is zero for isotropic materials and increases as symmetry decreases e.g. monoclinic and triclinic
275 minerals tend to have higher A^U .

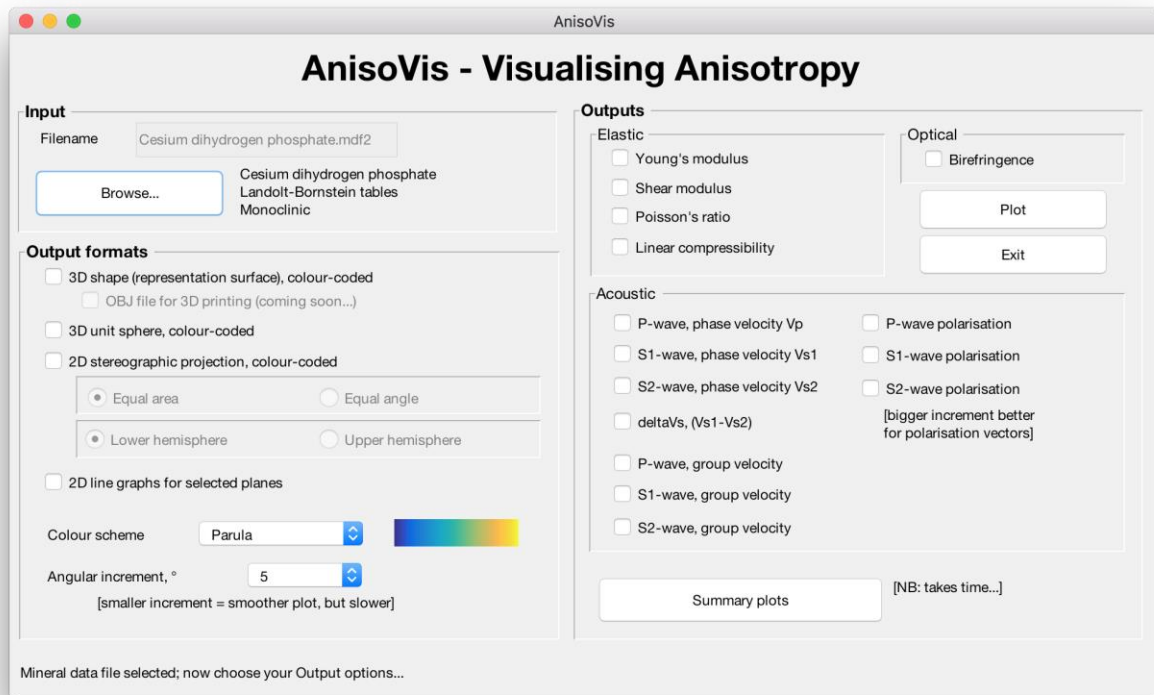
276

277 **3. AnisoVis – program description and visualisation methods**

278 The visualisations of elastic anisotropy presented in this paper have been prepared using AnisoVis,
279 a set of custom scripts linked to a graphical user interface (GUI) and written in MATLAB™. This
280 code is available as an open source project on GitHub (link) and through the MathWorks™
281 FileExchange server (<https://github.com/DaveHealy-Aberdeen/AnisoVis>;
282 <https://uk.mathworks.com/matlabcentral/fileexchange/73177-anisovis>). Single mineral elasticity
283 values are supplied as input data, together with lattice parameters defining the unit cell and
284 symmetry. The code then calculates the directional variations in elastic properties and produces
285 outputs of the kinds shown in Figures 4-7. AnisoVis can also calculate the acoustic velocities
286 (phase and group) and their polarisations, and the optical birefringence from the refractive indices.
287 Over 240 data files for 86 different minerals are included (from published sources), and a user guide
288 is provided with the software.

289 *Installation and input file format*

290 AnisoVis is installed by copying all of the files from the GitHub or Mathworks FileExchange server
291 into a folder on the user's computer. AnisoVis will run on any computer with MATLAB installed,
292 including running Windows, Mac OS X or different versions of Linux. After starting MATLAB, the
293 working folder or directory should be set to the folder containing the installed source code. The
294 application is started by typing 'AnisoVis' in the Command window of the MATLAB session.
295 There is only one window in AnisoVis (Figure 2). Click 'Browse...' to show the standard dialog to
296 open an input file of mineral properties. These data are stored in formatted tab-delimited ASCII text
297 files with an extension of '.mdf2' ('mineral data file'). The user guide supplied with the software
298 has examples for each different mineral symmetry class.



299

300 **Figure 2.** The graphical user interface in AnisoVis, showing the range of output options for elastic,
 301 acoustic and optical anisotropies.

302 *Calculations*

303 After selecting the required output formats (shape, sphere or stereogram) and anisotropic properties
 304 to be visualised (elastic, acoustic or optical), the user clicks Plot to generate the images.
 305 Calculations are performed using the equations for each property described above, looping through
 306 three-dimensional space with the specified angular increment. Smaller angular increments (e.g. 1-
 307 2°) take longer to run than larger increments (e.g. 5-10°). In the tests that we have conducted to
 308 date, run time has been very satisfactory, with most operations completed in a few seconds on
 309 standard desktop computers purchased within the last three years. The exception to this performance
 310 is when the angular increment is 1°, where run times are typically of the order of 1-2 minutes. We
 311 have implemented a MATLAB™ WaitBar to provide basic progress information for lengthier tasks.

312 *Generating outputs*

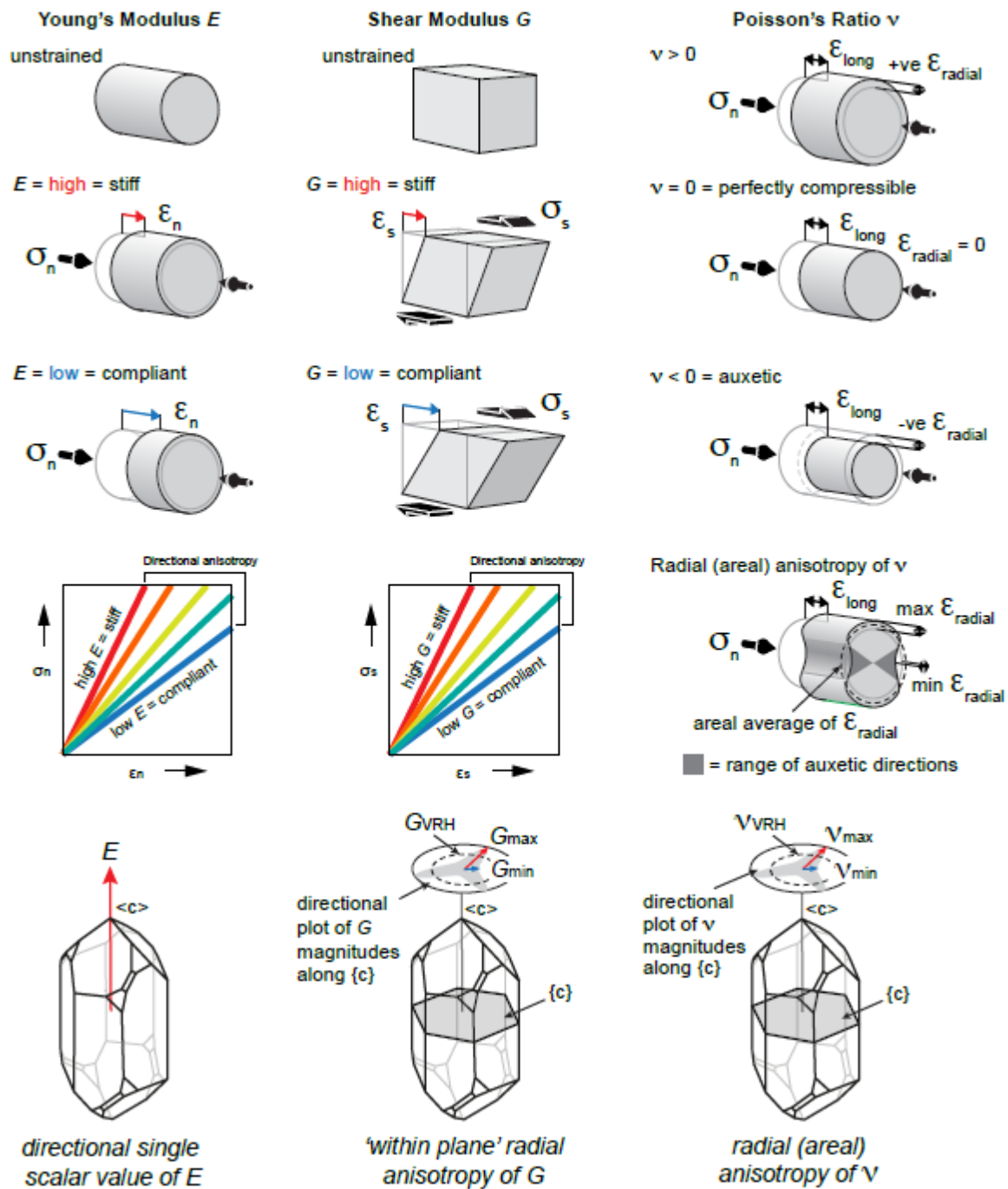
313 Output is directed to MATLAB figure windows, with one plotted property per figure window.
 314 These images are automatically saved as '.tif' files at 600 dpi resolution in the working folder.
 315 While each figure window is visible, the user can exploit standard MATLAB functionality to resize
 316 or reformat the figure as they wish, and can save the figure to a different filename or folder, or even
 317 a different graphic format (e.g. '.png' or '.jpeg'). The colour schemes used for the representation
 318 surfaces, unit spheres and stereograms can be varied using the drop-down list box in the main
 319 window. In addition to the standard MATLAB colour map of 'Parula' we offer 3 other choices from
 320 the cmocean colour map library (Thyng et al., 2016) using perceptually uniform scales ('Haline',
 321 'Thermal' and 'Matter').

322 *Visualising elastic anisotropy in 2-D and 3-D*

323 As pointed out by Nye (1985), no *single* surface can represent the elastic behaviour of a crystal
324 completely. However, we can plot specific surfaces that are useful in practice. To visualise the
325 anisotropy of elastic properties of single crystals we use a mixture of 3D surfaces and 2D polar
326 plots projected onto selected planes. We use representation surfaces (Nye, 1985) to generate 3D
327 shapes where, for any given radius vector measured from the origin to the surface, the radius is
328 proportional to the magnitude of the property in that direction. The magnitude of the property is
329 also conveyed by a colour mapping applied to the surface. An alternative method is to plot the
330 directional variation of a property projected onto a unit sphere, using a colour map to depict the
331 magnitude. We can also use stereographic projections (lower hemisphere, equal area) to show
332 directional variations in properties. Lastly, we can use polar plots to the variation of a property in
333 selected crystallographic planes (e.g. [100], [010], [001]).

334 *Challenges in visualising Poisson's ratio (ν) and shear modulus G*

335 Any of the above methods of visualisation can be used for 'simple' elastic properties, such as
336 Young's modulus or linear compressibility, where the property is a single scalar value for a given
337 direction. Young's modulus is defined as the ratio of uniaxial stress to uniaxial strain and it is
338 implicit that the directions of applied stress and measured strain are coincident (i.e. coaxial; Figure
339 3). However, for Poisson's ratio and shear modulus this is no longer the case. Poisson's ratio is
340 defined as the ratio of (negative) lateral strain to the axial strain, and therefore involves two
341 orthogonal directions (Figure 3). Shear modulus is defined as the ratio of the shear stress to the
342 shear strain, again involving two orthogonal directions (see Figure 3). For a stress (normal or shear)
343 applied in a specific direction, there is only one value of E , but there are many possible values of ν
344 and G . It can be seen from Figure 3 that ν and G will vary according to the direction of the normal
345 to the chosen direction $[hkl]$, described by angle θ in the Turley & Sines (1971) notation. To plot
346 representation surfaces for ν and G , we take their minimum and maximum values calculated over θ
347 for an applied stress along each direction in 3D-space. In addition, as ν can be negative for some
348 directions in some minerals, we further separate the minimum representation surfaces of Poisson's
349 ratio into negative minimum and positive minimum components where appropriate.

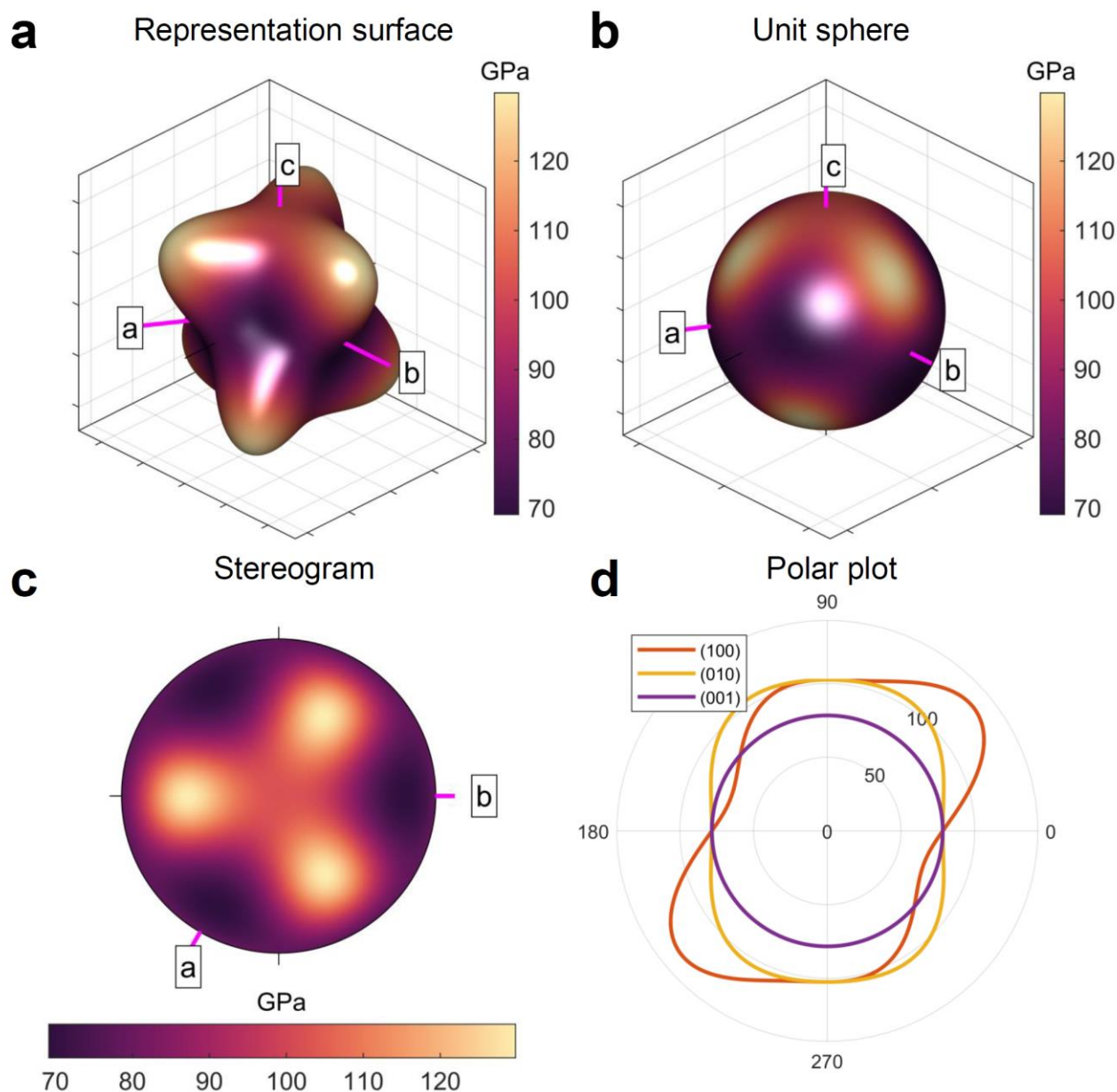


350

351 **Figure 3.** Schematic diagrams to illustrate the definitions of Young's modulus, Poisson's ratio,
 352 shear modulus in a 3D crystallographic reference frame, using α -quartz (trigonal) as an example.

353 *Example: α -quartz (trigonal; Ogi et al., 2006)*

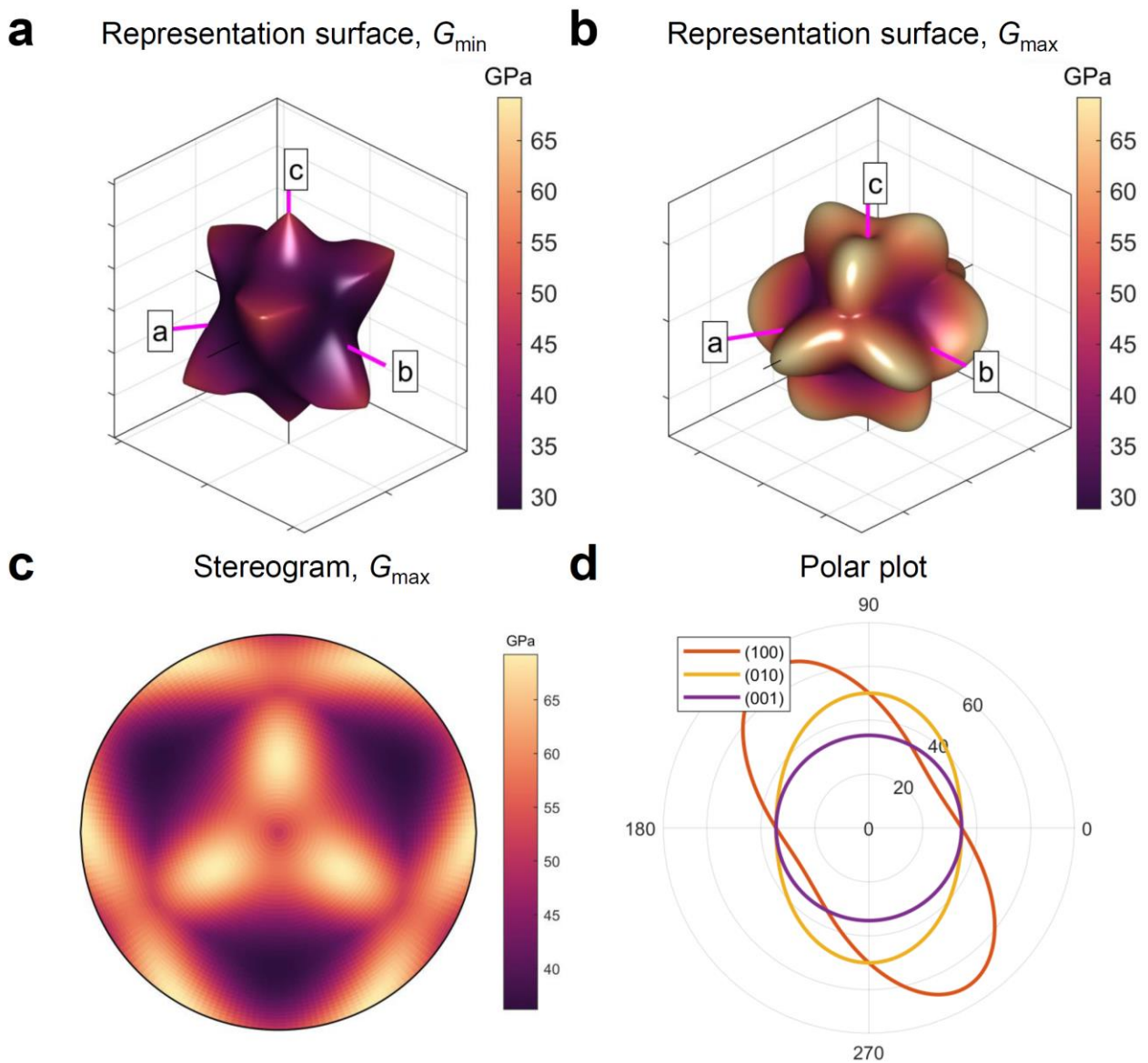
354 To illustrate the different possibilities described above we use the elasticity of α -quartz as
 355 quantified by Ogi et al. (2006). The anisotropy of Young's modulus is shown in Figure 4 using a
 356 representation surface, a unit sphere, a stereogram and polar plots of E in the plane (100). The
 357 colour bar scale is the same in all plots for ease of comparison. Using AnisoVis, the user can rotate
 358 any of these plot views in the MATLAB figures to gain a better appreciation of the directional
 359 variations in relation to the crystallographic reference axes $\langle a \rangle$, $\langle b \rangle$, and $\langle c \rangle$.



360

361 **Figure 4.** Alternative visualisations of the anisotropy of Young's modulus (E , in GPa) of α -quartz.
 362 **a)** 3D representation surface where the radius in any direction is proportional to the magnitude of E .
 363 **b)** Projection of E on to a unit sphere, colour-coded by magnitude. **c)** Lower hemisphere, equal area
 364 stereographic projection. **d)** Polar plot of anisotropy of E in selected planes. Crystallographic axes
 365 $\langle a \rangle$, $\langle b \rangle$, and $\langle c \rangle$ shown in pink.

366 As noted above, the shear modulus is a function of shear stress in one direction and a shear strain in
 367 a perpendicular direction. Therefore, for any given crystallographic direction in 3D space $[hkl]$ in an
 368 anisotropic crystal there are many possible values of G as the transverse component is rotated
 369 through the angle θ (see Figure 1b). In Figure 5 we show representation surfaces for the minimum
 370 and maximum values of G of α -quartz associated with each direction $[hkl]$. Polar plots are also
 371 shown for planes (010) and (001).

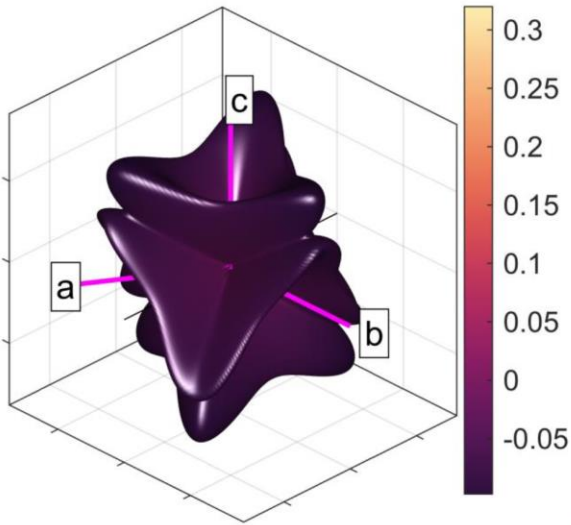


372

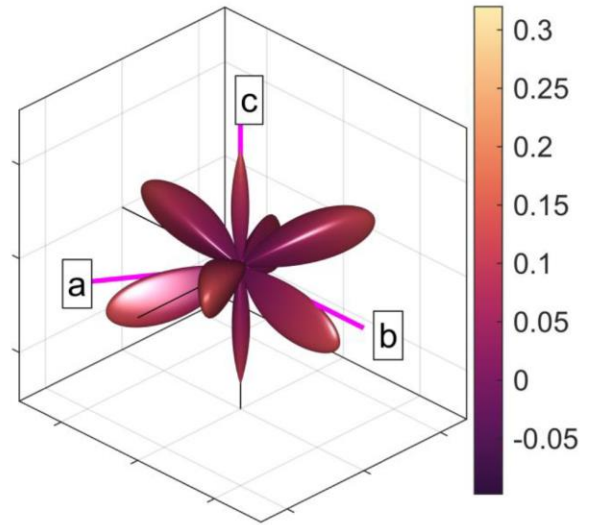
373 **Figure 5.** Alternative visualisations of the anisotropy of shear modulus (G , GPa) of α -quartz. **a-b)**
 374 3D representation surfaces where the radius in any direction is proportional to the magnitude of G .
 375 Separate surfaces shown for minimum and maximum G . **c)** Lower hemisphere, equal area
 376 stereographic projection of G_{\max} . **d)** Polar plots of anisotropy of G in selected planes.
 377 Crystallographic axes $\langle a \rangle$, $\langle b \rangle$, and $\langle c \rangle$ shown in pink. VRH = Voigt-Reuss-Hill average value of
 378 G .

379 Visualising the directional variation of Poisson's ratio ν can pose further challenges. α -quartz is
 380 auxetic and has many directions that show negative Poisson's ratios. As for shear modulus, we
 381 show representation surfaces for both the minimum (Figure 6a-b) and maximum (Figure 6c)
 382 Poisson's ratios, but we separate the minimum Poisson's ratio plot into two surfaces: one for $\nu_{\min} <$
 383 0 (Figure 6a) and one for $\nu_{\min} > 0$ (Figure 6b). Maximum Poisson's ratio is nearly always positive,
 384 and we show a single plot for this. We also include a plot for the areal Poisson's ratio – the value of
 385 Poisson's ratio averaged over all θ for each direction $[hkl]$ (Figure 6d, after Guo & Wheeler, 2006).
 386 Polar plots for specific 2D planes can also be useful (Figure 6e-f).

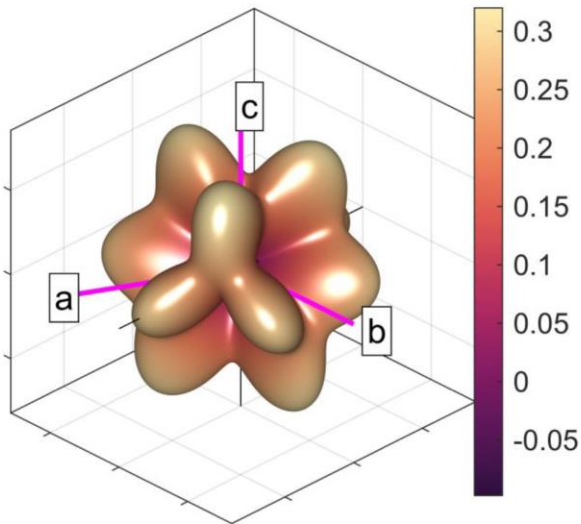
a Representation surface, $v_{\min} < 0$



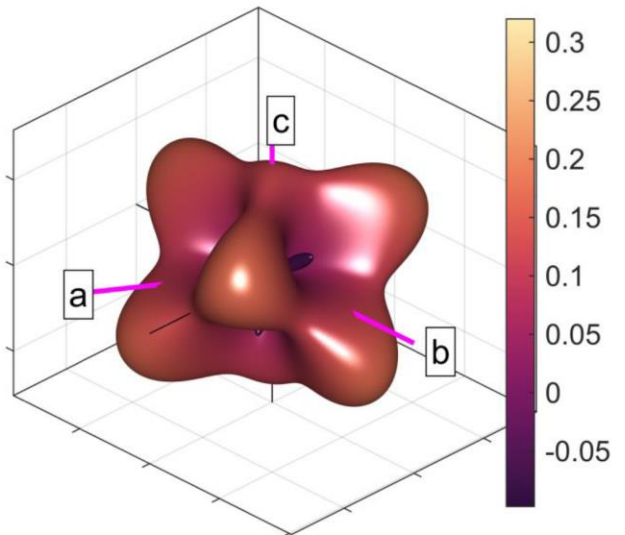
b Representation surface, $v_{\min} > 0$



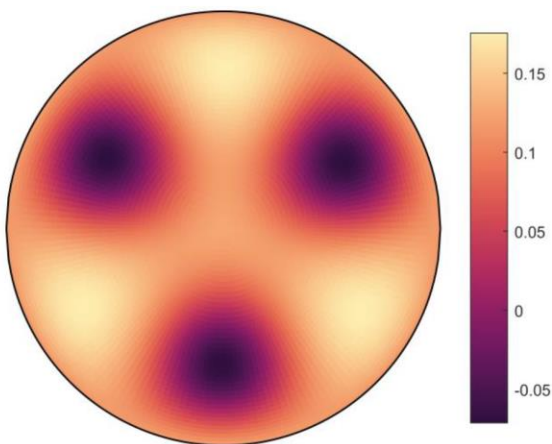
c Representation surface, v_{\max}



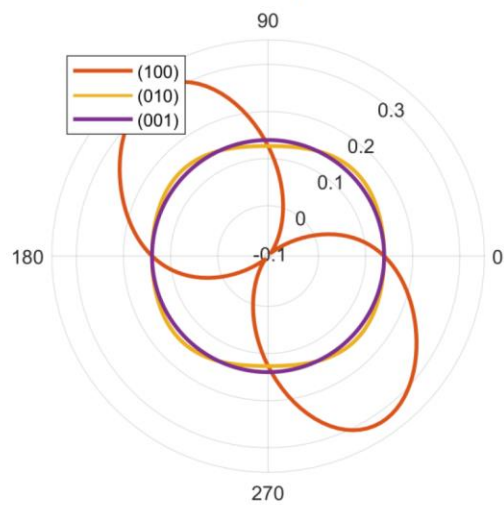
d Representation surface, v_{areal}



e Stereogram, v_{areal}

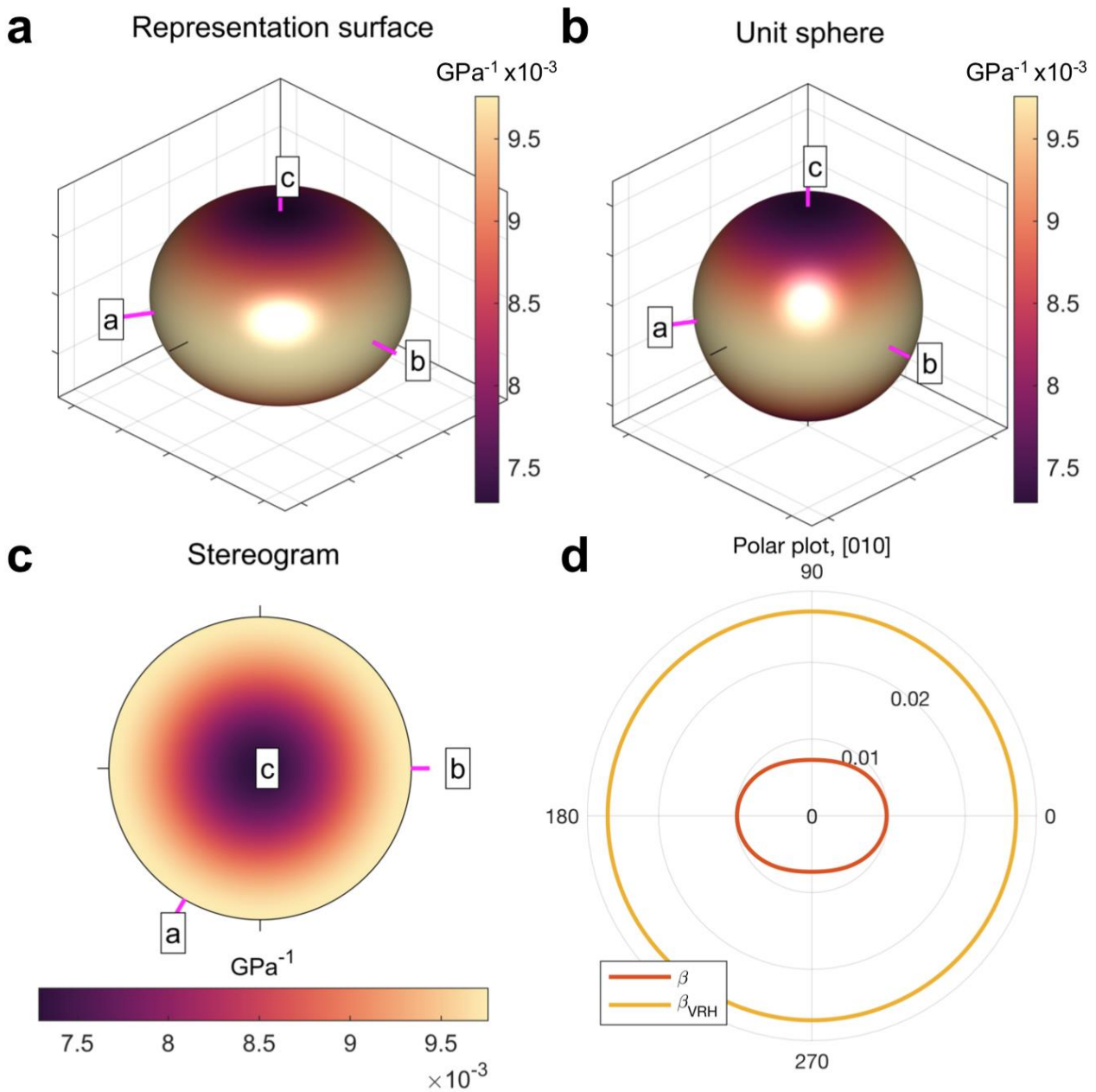


f Polar plot



388 **Figure 6.** Alternative visualisations of the anisotropy of Poisson's ratio (ν) of α -quartz. **a-d)** 3D
 389 representation surfaces where the radius in any direction is proportional to the magnitude of ν .
 390 Separate surfaces shown for minimum negative, minimum positive, maximum and areal ν , as
 391 defined in the equations in Section 2. **e)** Lower hemisphere, equal area stereographic projection of
 392 ν_{areal} . **f)** Polar plots of anisotropy of ν in selected planes. Crystallographic axes $\langle a \rangle$, $\langle b \rangle$, and $\langle c \rangle$
 393 shown in pink.

394



395

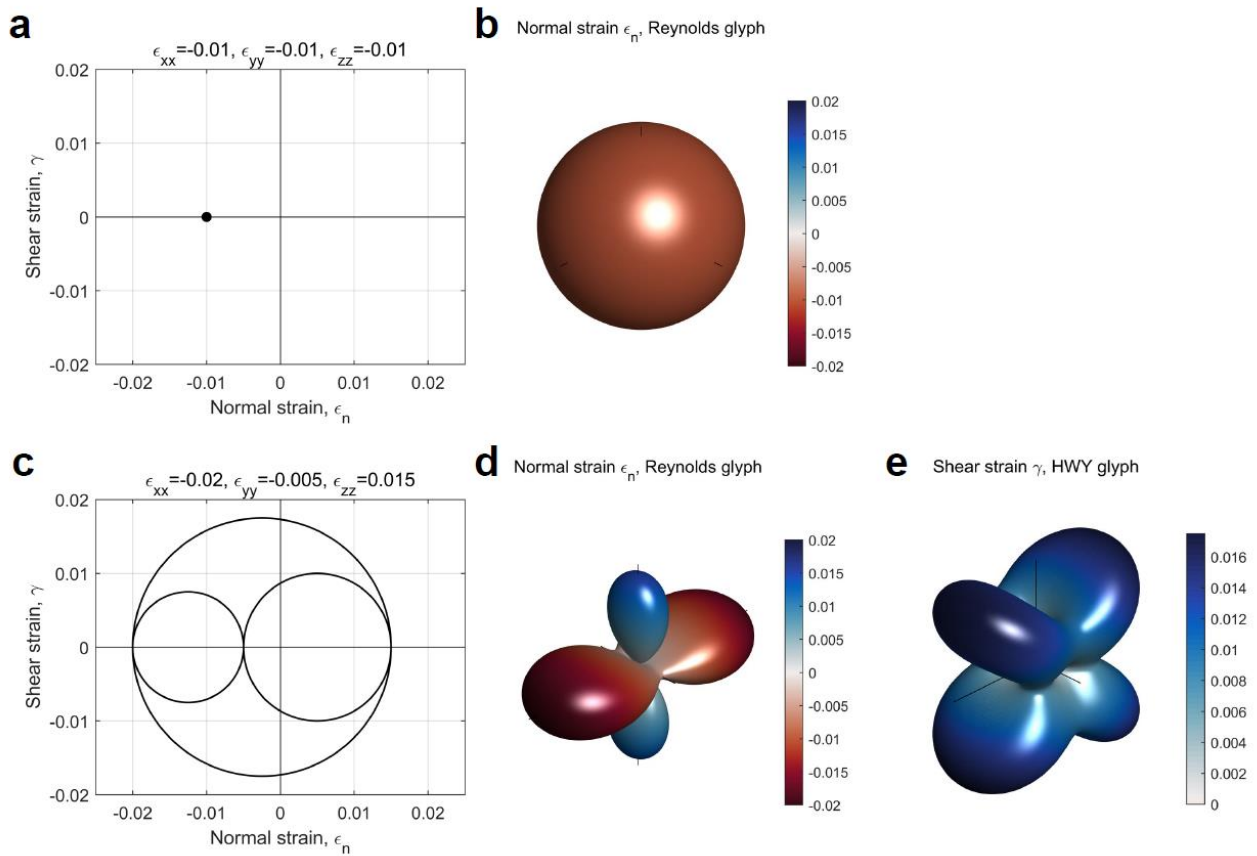
396 **Figure 7.** Alternative visualisations of the anisotropy of linear compressibility (β , in GPa^{-1}) of α -
 397 quartz. **a)** 3D representation surface where the radius in any direction is proportional to the
 398 magnitude of β . **b)** Projection of β on to a unit sphere, colour-coded by magnitude. **c)** Lower
 399 hemisphere, equal area stereographic projection. **d)** Polar plot of anisotropy of β in the (010) plane.
 400 Crystallographic axes $\langle a \rangle$, $\langle b \rangle$, and $\langle c \rangle$ shown in pink. VRH = Voigt-Reuss-Hill average value of
 401 β .

402 The linear compressibility (β) of an anisotropic crystal quantifies the directional response to an
403 applied hydrostatic load i.e. to pressure, not stress. For isotropic materials, the compressibility is a
404 scalar – i.e. directionally invariant – and is simply the inverse of the bulk modulus K ($\beta = 1 / K$).
405 For anisotropic rock-forming minerals, this is no longer the case and β varies with direction. Figure
406 7 shows the variation for α -quartz using the same types of plots as for Young's modulus (Figure 5).

407 In summary, we note that as a corollary of the point made by Nye (1985) that no single surface can
408 represent the full richness of the 4th rank elasticity tensor, neither can any one measure (e.g. E , G , ν
409 or β) convey the complete behavior of an anisotropic mineral. The anisotropies of the different
410 parameters shown in these plots should be used in combination to understand a specific problem.

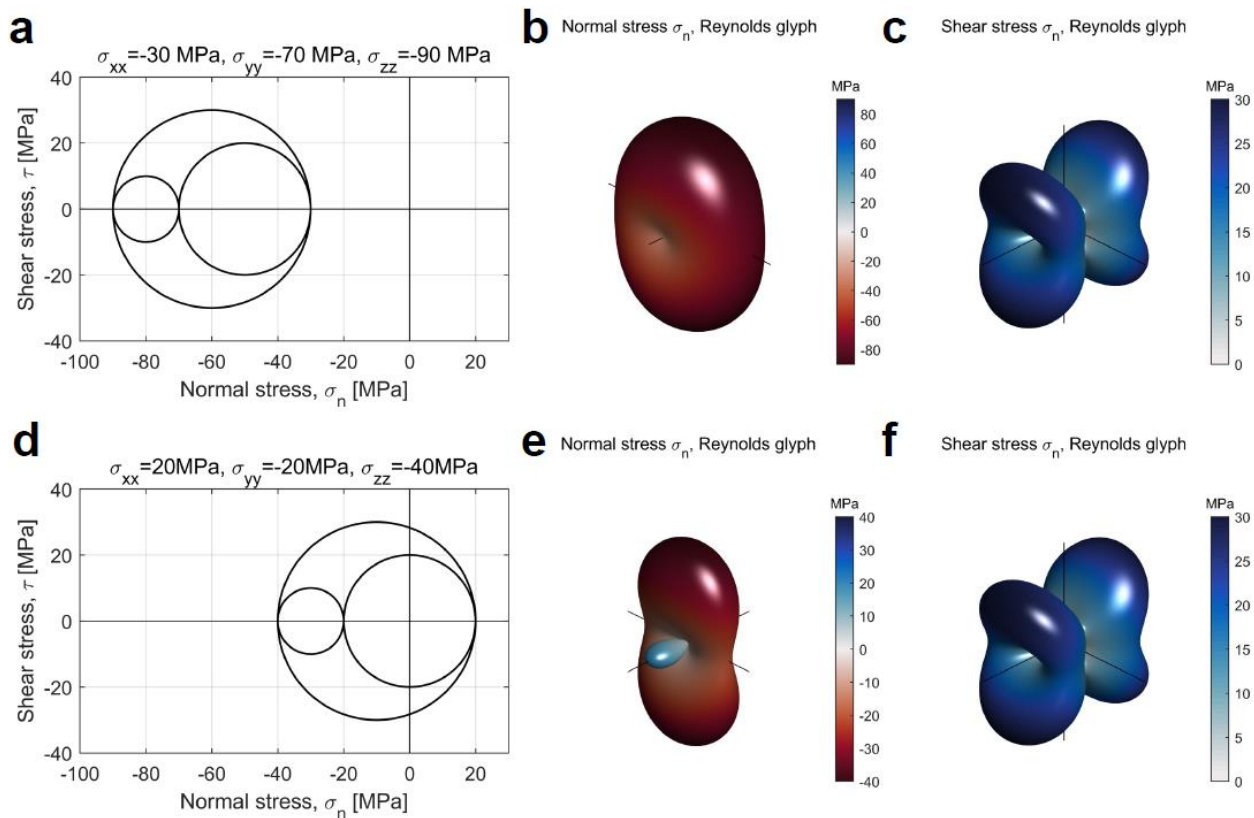
411 *Visualising second-rank tensors: stress and strain*

412 To address the challenges in visualizing stress and strain described above, we use two separate
413 graphical depictions, or glyphs, for the normal and shear components of the strain and stress tensors
414 (Kratz et al., 2014). We use the Reynolds glyph for normal strains and stresses, as this can show
415 positive and negative principal values (Moore et al., 1996). We use the HWY glyph to visualise the
416 shear components of the strain and stress tensors (Hashash et al., 2003). Figures 8 and 9 show
417 examples of the Reynolds and HWY glyphs for strains and stresses, respectively. Isotropic
418 compaction plots as a single point in Mohr space (Figure 8a), and as a sphere using a Reynolds
419 glyph (Figure 8b; shear strains are zero and so there is no HWY glyph). For a general triaxial strain
420 with both shortening and stretching components, the Reynolds and HWY glyphs are shown in
421 Figure 8d and 8e. Note that in the HWY glyph for shear strain the maxima are located at 45° to the
422 principal axes, and the minima (0) are located along the principal axes. Triaxially compressive
423 stress is shown in Figure 9a-c. Again, maxima of shear stress in the HWY glyph are at 45° to the
424 directions of the principal (normal) stresses. For a general triaxial stress with components of
425 compression and tension, the directional variations of normal and shear stress are shown in Figure
426 9d-f.



427

428 **Figure 8.** Examples of strain tensors depicted in Mohr space (ϵ_n, γ), and as Reynolds (normal
 429 strains, ϵ_n) and HWY (shear strains, γ) glyphs. **a-b)** Isotropic compaction (taken as negative, blue
 430 colour). **c-e)** Visualisations for a general triaxial strain. Note the lobes of extensional (blue) and
 431 contractional (red) strain in the normal strain plot (**d**).



432

433 **Figure 9.** Examples of stress tensors depicted in Mohr space (σ_n , τ) and as Reynolds (normal stress, σ_n) and HWY (shear stress, τ) glyphs. **a-c)** Triaxial compression (taken as negative, blue colour).
 434 σ_n) and HWY (shear stress, τ) glyphs. **a-c)** Triaxial compression (taken as negative, blue colour).
 435 **d-f)** General triaxial stress with one principal stress tensile (σ_{xx}).

436

437 4. Results – General trends

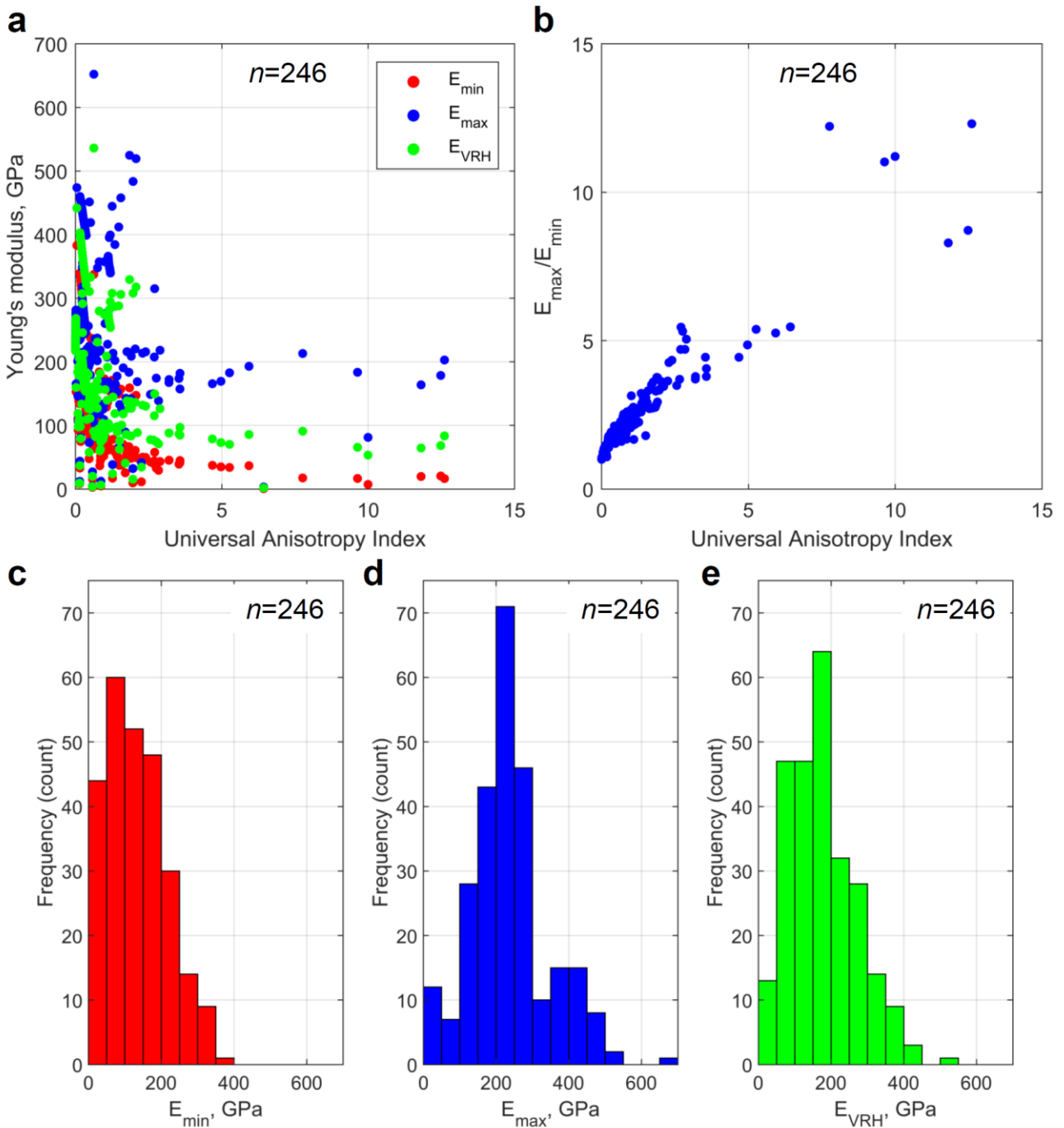
438 *Data sources*

439 The elastic properties of the minerals used in this study have been derived from previous
 440 compilations and original sources where possible. Many compilations of elastic and other physical
 441 properties are now available: see Bass (1995) and Almqvist & Mainprice (2017), and references
 442 therein. Note that most elastic properties are measured by laboratory methods whereas a minority
 443 are calculated from theory (*ab initio* molecular dynamics simulations; e.g. Mainprice et al., 2018).
 444 Single mineral lattice parameters have been extracted from the same publication as the elasticity
 445 data where possible, but if this was not available, we took representative values from Deer, Howie
 446 & Zussman (1992).

447 *Summary plots*

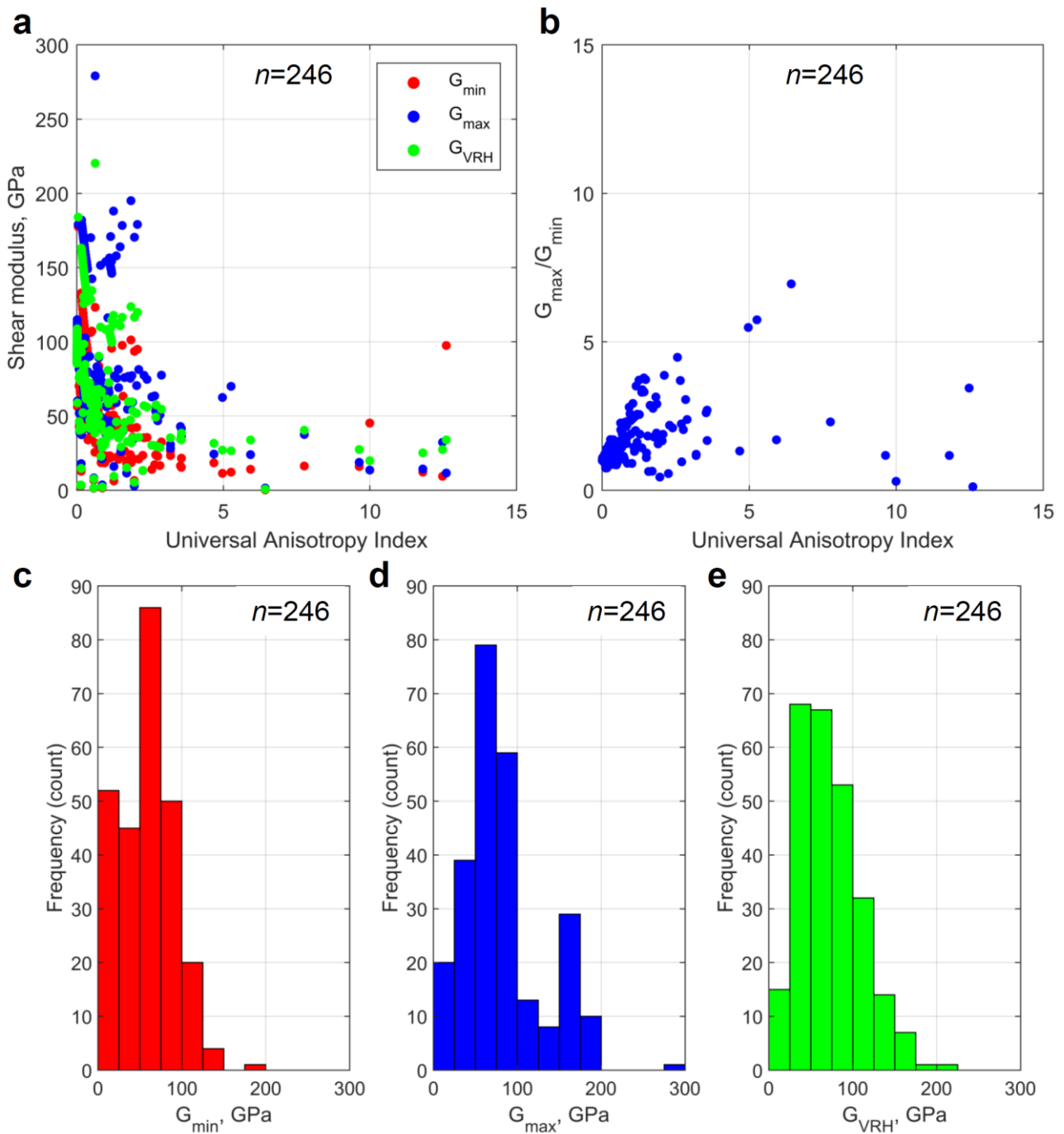
448 From our database of published elastic properties of rock-forming minerals (246 data files covering
 449 86 distinct minerals, all included with AnisoVis), we have calculated the maxima and minima for
 450 Young's modulus, Poisson's ratio, shear modulus and linear compressibility. In Figure 10 we show
 451 the variation in the anisotropy of Young's modulus (E) for 246 rock-forming minerals as a function
 452 of the Universal Anisotropy Index A^U . If we consider a simple measure of the anisotropy of E as the
 453 ratio between the maximum and minimum values, it is clear that most minerals display significant

454 anisotropy with E_{max}/E_{min} often greater than 2. With increasing A^U , many minerals show E_{max}/E_{min}
 455 ratios of about 4 or more. Figure 11 shows the anisotropy of shear modulus (G) for the same rock-
 456 forming minerals, plotted against A^U . The anisotropy of G , simply defined as G_{max}/G_{min} , is less than
 457 that shown for E , and this ratio tends to flatten out with increasing A^U .



458

459 **Figure 10.** Anisotropy of Young's modulus in rock-forming minerals ($n=246$) plotted against the
 460 Universal Anisotropy Index (A^U) of Ranganathan & Ostoja-Starzewski (2008). E_{VRH} is the Voigt-
 461 Reuss-Hill average of E . Many minerals display anisotropy of E (E_{max}/E_{min}) of 2 or more. **b)** Plot of
 462 E_{max}/E_{min} versus A^U . **c-e)** Histograms of E_{min} , E_{max} and E_{VRH} to show the distribution across all 246
 463 datasets.

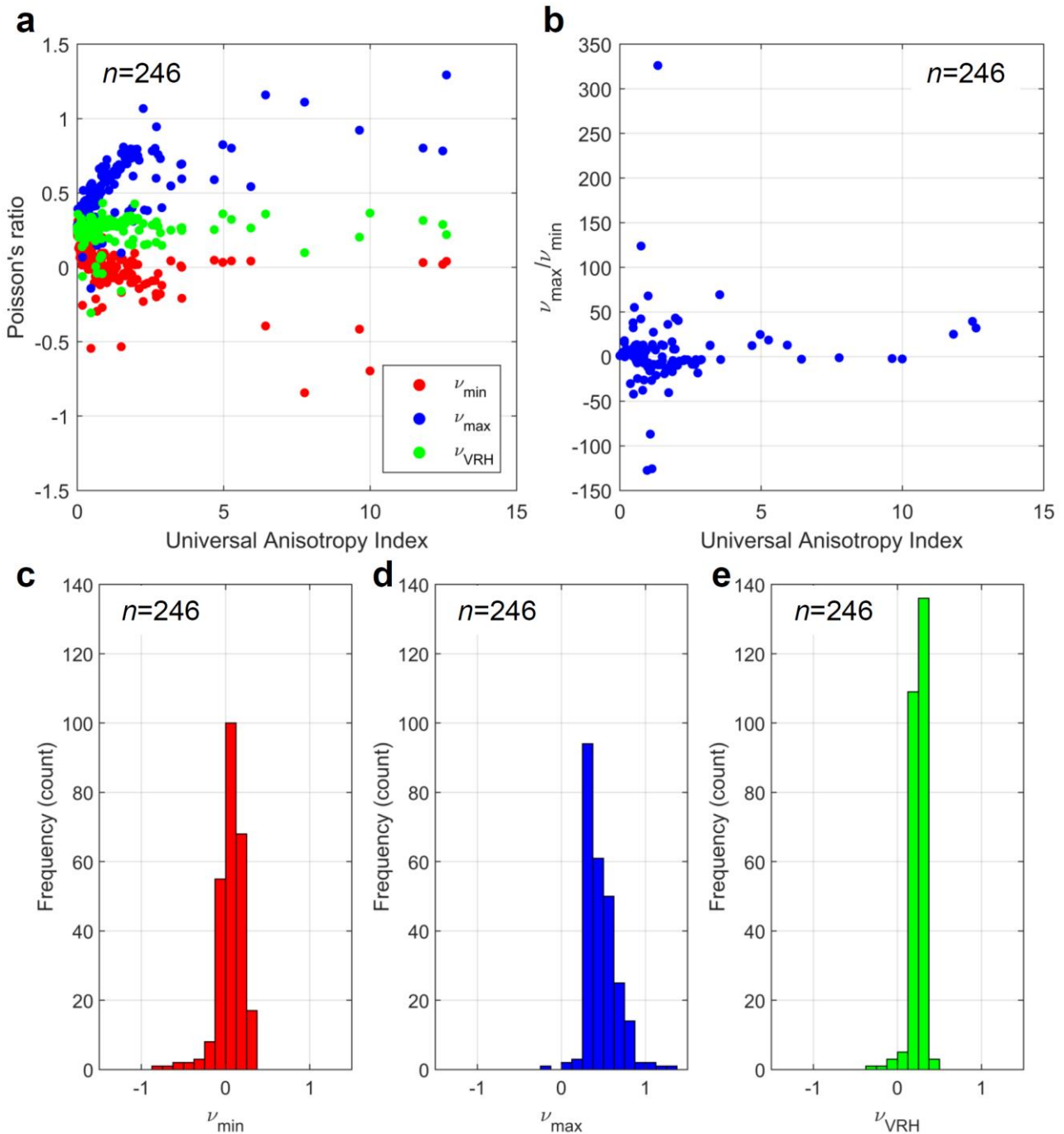


464

465 **Figure 11.** Anisotropy of shear modulus in rock-forming minerals ($n=246$) plotted against the
 466 Universal Anisotropy Index of Ranganathan & Ostoja-Starzewski (2008). G_{VRH} is the Voigt-Reuss-
 467 Hill average of G . **b)** Plot of G_{max}/G_{min} versus A^U . **c-e)** Histograms of G_{min} , G_{max} and G_{VRH} to show
 468 the distribution across all 246 datasets.

469 Figure 12 shows the variation in Poisson's ratio (ν) versus A^U for all minerals. The shaded area in
 470 Figure 12a and 12b denotes the range $0 \leq \nu \leq 0.5$. As noted by Ting & Chen (2005), ν for
 471 anisotropic materials can have no bounds. The data show that many minerals have minimum values
 472 less than 0 and maximum values greater than 0.5. The histogram in Figure 12c shows the statistical
 473 variation in ν_{min} for all minerals: 28% ($=70/246$) have negative minimum values for Poisson's ratio
 474 – that is, they display auxetic behaviour. Analysis of the variation of ν_{max} shows that 37% ($=91/246$)
 475 have values greater than 0.5 (Figure 12d). The mean value of the Voigt-Reuss-Hill average of

476 Poisson's ratio for all minerals is 0.2464 (Figure 12e), close to the default assumption of many
 477 simplifications to elastic isotropy ($\nu=0.25$). A full list of the rock-forming minerals in our database
 478 that show auxetic behaviour is shown in Table 2, and the specific directions of negative ν are shown
 479 for several examples in the stereograms in Figure 13.



480
 481 **Figure 12.** a) Anisotropy of Poisson's ratio in rock-forming minerals (n=246) plotted against the
 482 Universal Anisotropy Index of Ranganathan & Ostoja-Starzewski (2008). ν_{VRH} is the Voigt-Reuss-
 483 Hill average of ν . b) Plot of ν_{\max}/ν_{\min} versus A^U . c) Histogram of ν_{\min} values shown in Figure 12.
 484 Note that 28% (n=70/246) of minerals display negative ν_{\min} . d) Histogram of ν_{\max} values. 37%
 485 (n=91/246) minerals display $\nu_{\max} > 0.5$. e) Histogram of ν_{VRH} values. Mean $\nu_{\text{VRH}} = 0.2464$, very
 486 close to the common default assumption of $\nu = 0.25$.

487

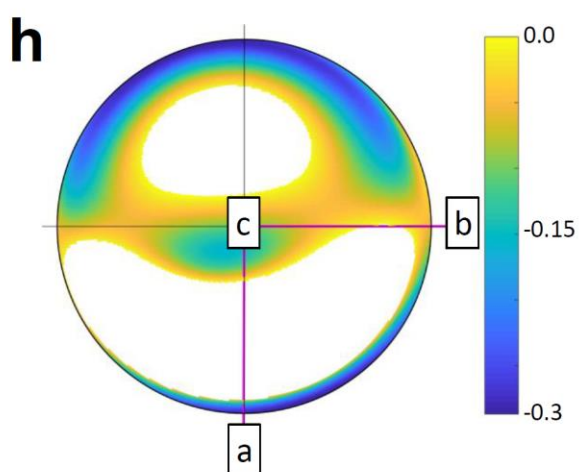
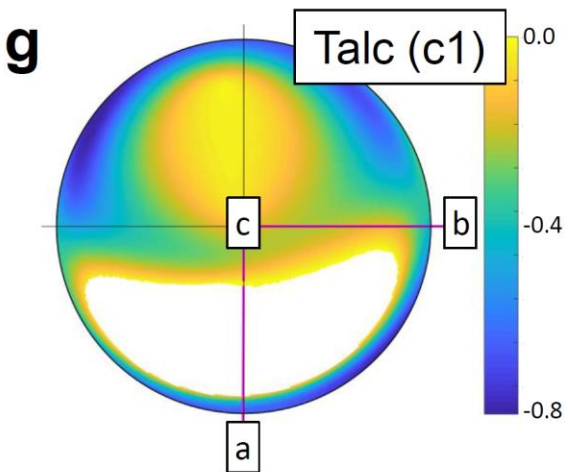
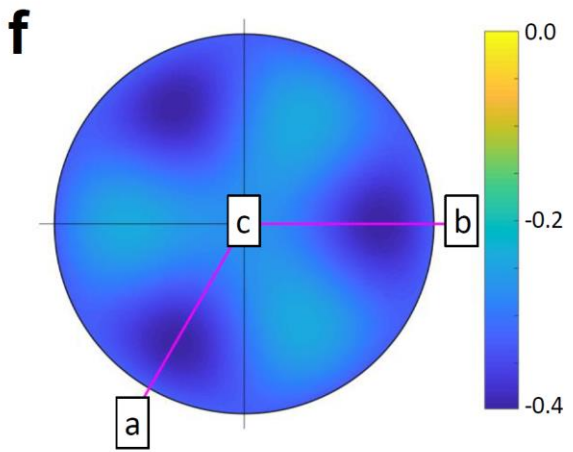
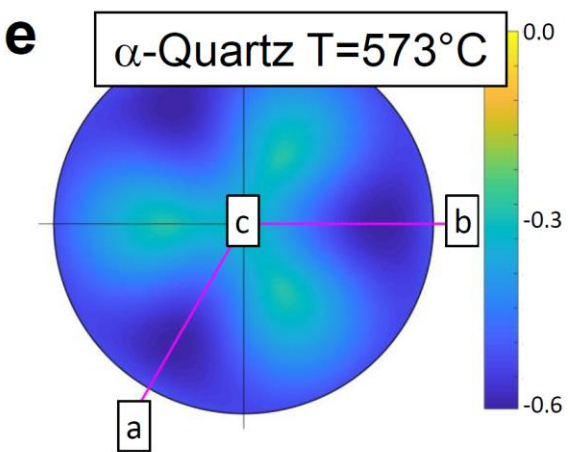
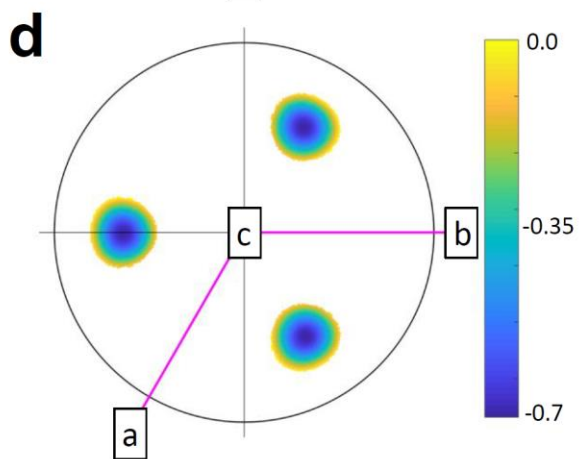
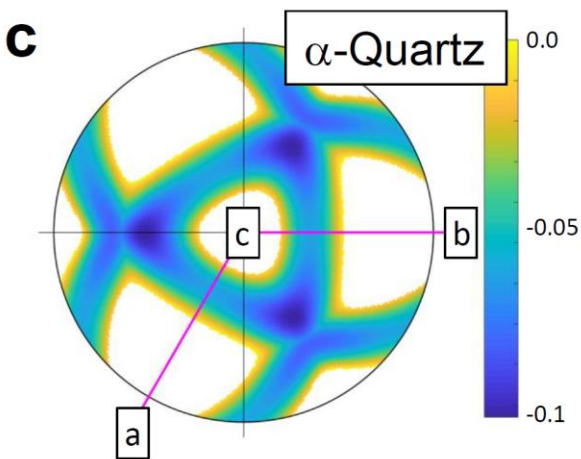
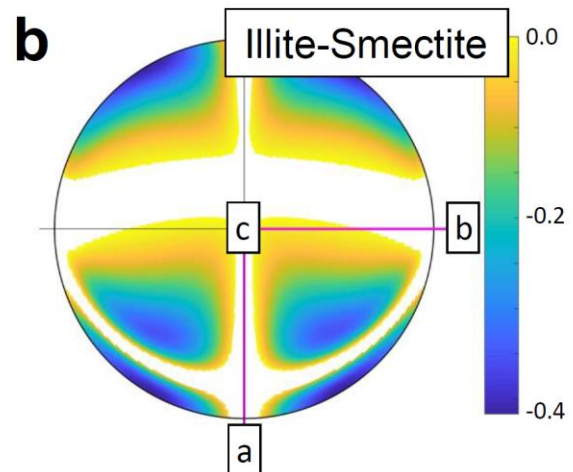
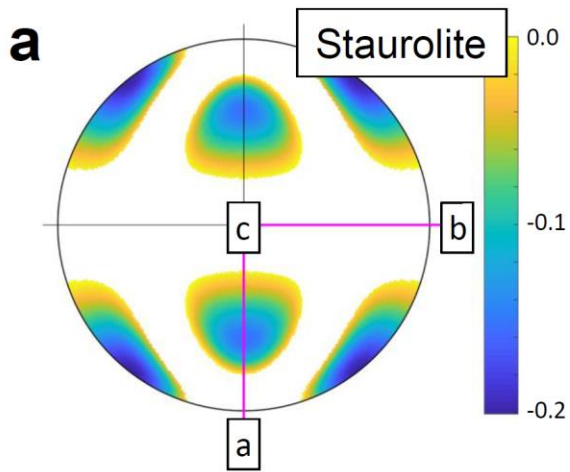
Mineral	Symmetry	Minimum $\nu < 0$	Minimum areal $\nu < 0$	Reference
Albite (An0)	Triclinic	-0.03		Hearmon, 1984
	Triclinic	-0.15		Brown et al., 2016
Anhydrite	Orthorhombic	-0.046		Hearmon, 1979
Andesine (An37)	Triclinic	-0.091		Brown et al., 2016
Andesine (An48)	Triclinic	-0.075		Brown et al., 2016
Antigorite	Monoclinic	-0.215		Bezacier et al., 2010
Aragonite	Orthorhombic	-0.061		Hearmon, 1979
Augite	Monoclinic	-0.012		Alexandrov et al., 1964
Bytownite (An78)	Triclinic	-0.053		Brown et al., 2016
Calcite	Trigonal	-0.047		Babuska & Cara, 1991
	Hexagonal	-0.02		Chen et al., 2001
Coesite	Monoclinic	-0.108		Weidner & Carleton, 1977
α -Cristobalite	Tetragonal	-0.537	-0.262	Pabst & Gregorova, 2013
β -Cristobalite	Cubic	-0.288	-0.162	Pabst & Gregorova, 2013
Dolomite	Trigonal	-0.064		Hearmon, 1979
Hornblende	Monoclinic	-0.075		Hearmon, 1984
Illite-Smectite	Monoclinic	-0.416		Militzer et al., 2011
Labradorite	Triclinic	-0.085		Ryzhova, 1964
Labradorite (An60)	Triclinic	-0.009		Brown et al., 2016
Labradorite (An67)	Triclinic	-0.025		Brown et al., 2016
Lawsonite	Orthorhombic	-0.088		Sinogeikin et al., 2000
Microcline	Triclinic	-0.199	-0.042	Babuska & Cara, 1991
Oligoclase (An25)	Triclinic	-0.098		Brown et al., 2016
Orthoclase	Monoclinic	-0.169		Hearmon, 1984
	Monoclinic	-0.092		Waesermann et al., 2016
α -Quartz	Trigonal	-0.97	-0.071	Ogi et al., 2006
	Trigonal	-0.93	-0.067	Babuska & Cara, 1991
T=200°C	Trigonal	-0.123	-0.088	Lakshtanov et al., 2007
T=400°C	Trigonal	-0.215	-0.138	Lakshtanov et al., 2007
T=500°C	Trigonal	-0.301	-0.186	Lakshtanov et al., 2007
T=573°C	Trigonal	-0.546	-0.398	Lakshtanov et al., 2007
T=575°C	Hexagonal	-0.255	-0.095	Lakshtanov et al., 2007
Rutile	Tetragonal	-0.044		Manghnani, 1969
Sanidine	Monoclinic	-0.097		Waesermann et al., 2016
Sillimanite	Orthorhombic	-0.001		Verma, 1960
Sphalerite	Cubic	-0.025		Hearmon, 1984
Spinel	Cubic	-0.07		Hearmon, 1984
T=300°K	Cubic	-0.081		Anderson & Isaak, 1995
T=350°K	Cubic	-0.079		Anderson & Isaak, 1995
T=400°K	Cubic	-0.083		Anderson & Isaak, 1995
T=450°K	Cubic	-0.083		Anderson & Isaak, 1995
T=500°K	Cubic	-0.084		Anderson & Isaak, 1995
T=550°K	Cubic	-0.084		Anderson & Isaak, 1995

T=600°K	Cubic	-0.085		Anderson & Isaak, 1995
T=650°K	Cubic	-0.033		Anderson & Isaak, 1995
T=700°K	Cubic	-0.088		Anderson & Isaak, 1995
T=750°K	Cubic	-0.089		Anderson & Isaak, 1995
T=800°K	Cubic	-0.09		Anderson & Isaak, 1995
T=850°K	Cubic	-0.092		Anderson & Isaak, 1995
T=900°K	Cubic	-0.093		Anderson & Isaak, 1995
T=950°K	Cubic	-0.094		Anderson & Isaak, 1995
T=1000°K	Cubic	-0.095		Anderson & Isaak, 1995
Staurolite	Orthorhombic	-0.201		Hearmon, 1979
Stishovite	Tetragonal	-0.04		Babuska & Cara, 1991
Talc (c1)	Triclinic	-0.864	-0.287	Mainprice et al., 2008
P=0.87 GPa	Triclinic	-0.178	-0.001	Mainprice et al., 2008
P=1.96 GPa	Triclinic	-0.107		Mainprice et al., 2008
P=3.89 GPa	Triclinic	-0.009		Mainprice et al., 2008
Talc (c2c)	Monoclinic	-0.126	-0.029	Mainprice et al., 2008
P=0.15 GPa	Monoclinic	-0.107	-0.021	Mainprice et al., 2008
P=0.35 GPa	Monoclinic	-0.125	-0.025	Mainprice et al., 2008
P=0.64 GPa	Monoclinic	-0.091	-0.002	Mainprice et al., 2008
P=0.93 GPa	Monoclinic	-0.028		Mainprice et al., 2008
P=1.72 GPa	Monoclinic	-0.019		Mainprice et al., 2008
Zircon (metamict)	Tetragonal	-0.113		Hearmon, 1984
Zoisite	Orthorhombic	-0.014		Mao et al., 2007
Number of distinct minerals		<i>n</i> =33	<i>n</i> =7	

488

489 **Table 2.** List of rock-forming minerals showing auxetic behaviour (Poisson's ratio < 0) in at least
490 one direction. Also shown are those minerals with directions that have negative areal Poisson's ratio
491 (Guo & Wheeler, 2006). The Reference column shows the source of the elasticity data for each
492 mineral used in the calculation. The auxetic directions were found by calculating Poisson's ratio for
493 every possible direction (α , β , θ in the Turley & Sines reference frame shown in Figure 1) using an
494 angular increment of 1 degree in each direction.

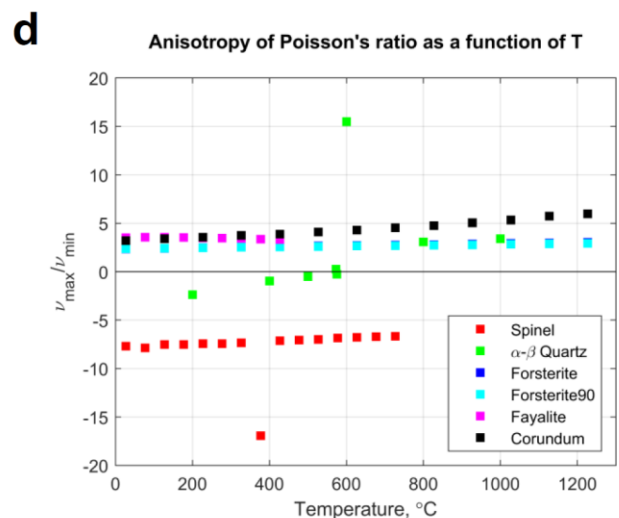
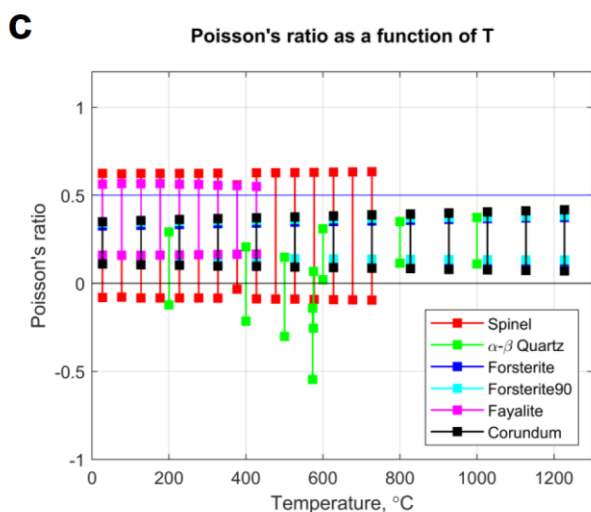
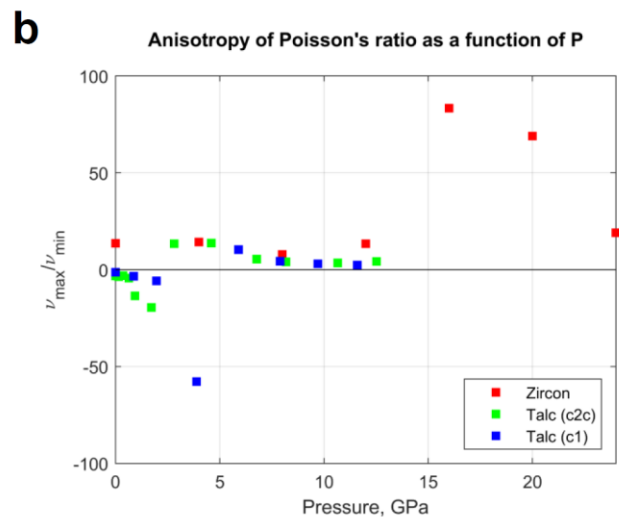
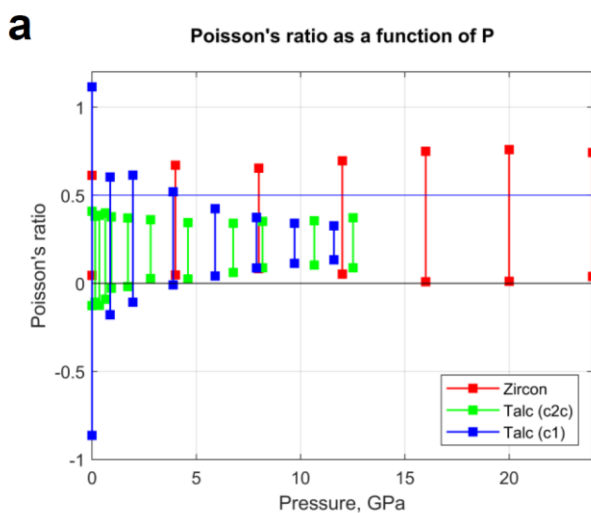
495



497 **Figure 13.** Examples of rock-forming minerals showing auxetic and areally auxetic behaviour.
 498 Stereograms are all lower hemisphere, equal area projections and only the directions with negative
 499 Poisson's ratio (a, b, c, e, g) or negative areal Poisson's ratio (d, f, h) are shown coloured in (i.e.
 500 other directions show positive values). Crystallographic axes in pink. **a)** Staurolite. **b)** Illite-
 501 smectite. **c-d)** α -Quartz. **e-f)** α -Quartz at the temperature of the phase transformation to β -Quartz
 502 (hexagonal). **g-h)** Talc (c1, triclinic).

503

504 The elastic properties of minerals are known to be temperature (T) and pressure (P) dependent.
 505 However, systematic data to quantify the variation of anisotropic elasticity with T or P is relatively
 506 scarce. We summarise some of the published data in Figure 14, shown as the calculated range in
 507 Poisson's ratio (ν_{min} to ν_{max}). In terms of pressure dependence, the effect of increasing P is to
 508 decrease the anisotropy in ν for talc to within the range normally expected for isotropic minerals.
 509 The opposite effect is observed for zircon, with modest increases in ν_{max} with P . The temperature
 510 dependence of elastic anisotropy in quartz is well known (Mainprice & Casey, 1990), with a
 511 significant excursion into auxetic behaviour at the temperature of the α - β phase transition at 573°C
 512 (846°K). The effect of increasing T on the anisotropy of ν for olivine, corundum and spinel is
 513 almost non-existent.



514

515 **Figure 14.** Anisotropy of Poisson's ratio in rock-forming minerals as a function of P (top) and T
 516 (bottom). Other than the well-known auxeticity of α - β quartz around the phase transition
 517 ($T=573^\circ\text{C}$), most minerals display Poisson's ratios of between 0-0.5. Talc (c1, triclinic) is one
 518 exception, and the anisotropy of Poisson's ratio decreases markedly with increasing P .

519 Linear compressibility (β) also displays significant anisotropy in rock-forming minerals (Figure
 520 16). A list of the rock-forming minerals in our database that show negative linear compressibility
 521 (NLC) is shown in Table 3. These minerals have directions that expand in response to a
 522 compressive hydrostatic pressure (and vice versa: 'stretch-densification' of Baughman et al.,
 523 1998b). The specific directions of negative β are shown in the stereograms in Figure 15.

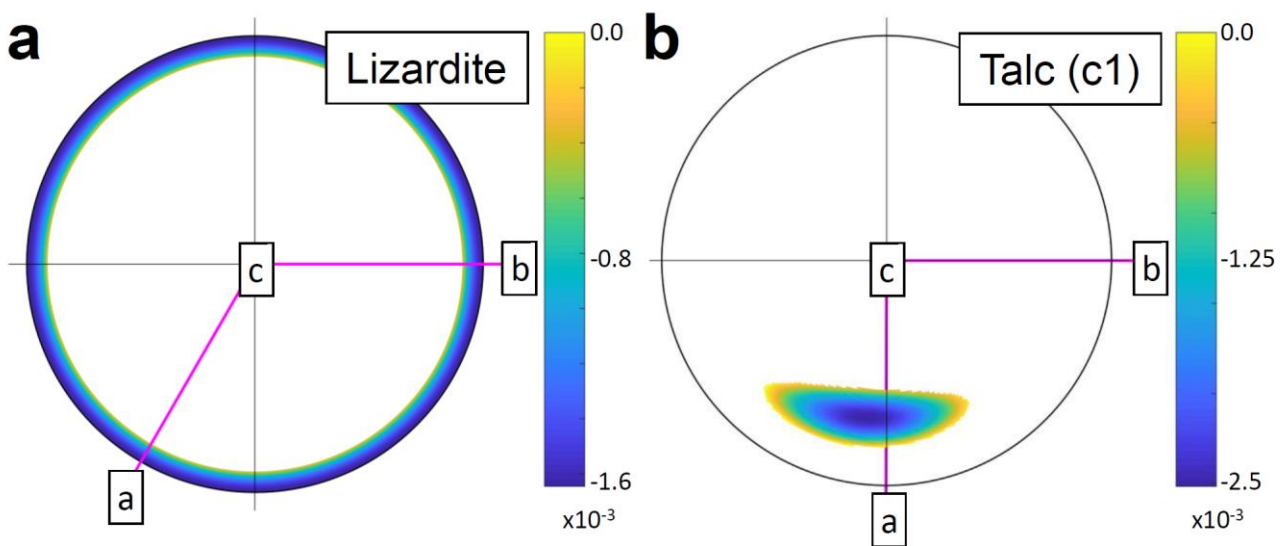
524

Mineral	Symmetry	Minimum $\beta < 0$, GPa^{-1}	Reference
Lizardite	Hexagonal	-0.00165	Reynard et al., 2007
Talc (c1)	Triclinic	-0.00251	Mainprice et al., 2008

525

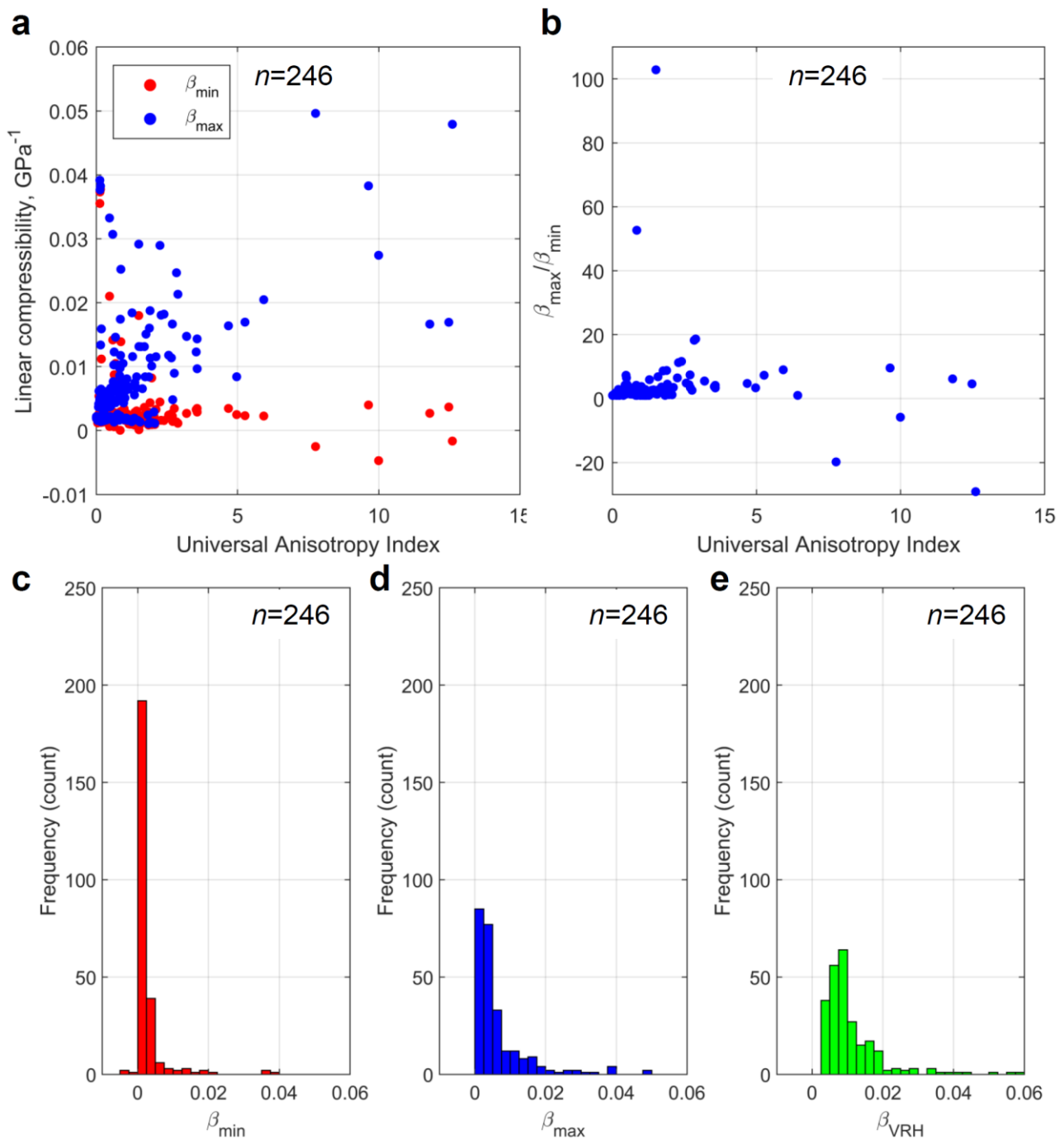
526 **Table 3.** List of rock-forming minerals showing negative linear compressibility (NLC) in at least
 527 one direction.
 528

529



529

530 **Figure 15.** Rock-forming minerals showing negative linear compressibility (NLC) in certain
 531 directions. Stereograms are all lower hemisphere, equal area projections and only the directions
 532 with NLC are shown coloured in (i.e. other directions show positive values). Crystallographic axes
 533 in pink. **a)** Lizardite. **b)** Talc (c1, triclinic).



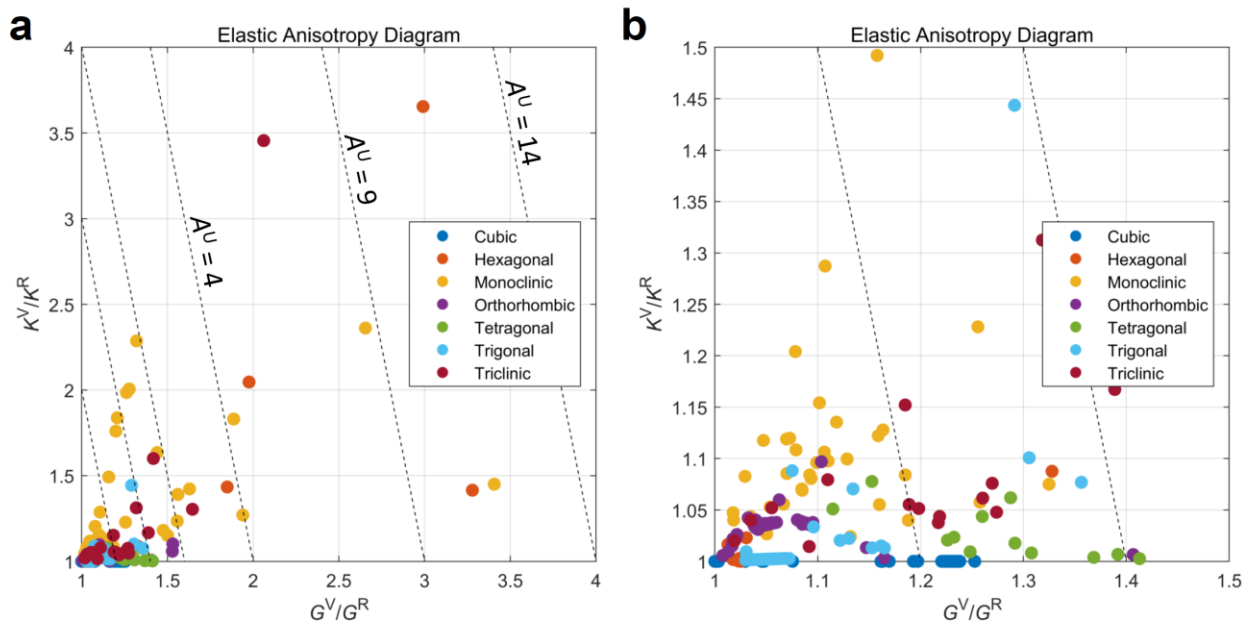
534

535 **Figure 16. a)** Anisotropy of linear compressibility (β , GPa^{-1}) in rock-forming minerals ($n=246$)
 536 plotted against the Universal Anisotropy Index of Ranganathan & Ostoja-Starzewski (2008). **b)** Plot
 537 of $\beta_{\max}/\beta_{\min}$ versus A^U . **c-e)** Histograms of β_{\min} , β_{\max} and β_{VRH} to show the distribution across all 246
 538 datasets.

539

540 We can summarise the elastic anisotropy data for all rock-forming minerals using the Elastic
 541 Anisotropy Diagram of Ranganathan & Ostoja-Starzewski (2008). In their review of Poisson's ratio
 542 in materials, Greaves et al. (2011) used a plot of bulk modulus K versus shear modulus G , however
 543 for the anisotropic rock-forming minerals there is no single value of either of these properties.
 544 Following Ranganathan & Ostoja-Starzewski (2008), we therefore take the ratios K^V/K^R and G^V/G^R
 545 and cross-plot these instead (Figure 17). Note that the origin is at (1,1) as no mineral can have

546 $K^V/K^R < 1$ or $G^V/G^R < 1$. The dashed lines of slope -5 are for constant A^U (equation 14), increasing
 547 to the right. Unsurprisingly, minerals with monoclinic, triclinic and hexagonal symmetries dominate
 548 the higher elastic anisotropies, while minerals with cubic, orthorhombic and tetragonal symmetries
 549 are generally less elastically anisotropic.



550

551 **Figure 17. a)** Anisotropy of rock-forming minerals ($n=246$) using the Elastic Anisotropy Diagram
 552 used in materials science, grouped by mineral symmetry class. **b)** Close-up of the data plotted in a),
 553 in the range G^V/G^R 1 to 1.5 and K^V/K^R 1 to 1.5.

554

555 5. Results – Specific examples

556 *Twinning*

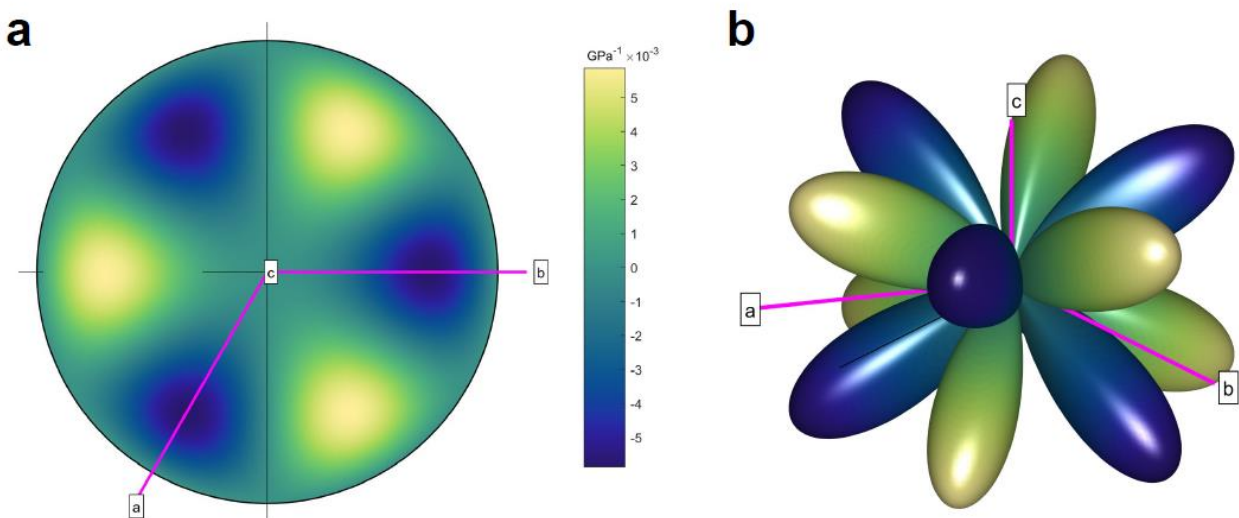
557 Deformation or mechanical twinning critically depends on the anisotropy of elastic properties
 558 because minerals respond elastically to imposed stress (or strain) before exceeding the threshold for
 559 twin nucleation and propagation (Christian and Mahajan, 1995, and references therein). Perhaps the
 560 most widely accepted theory is that twin initiation occurs when an applied shear stress along the
 561 twin shear plane (K_1) in the shear direction of twinning (η_1) reaches a critical value (critically
 562 resolved shear stress, CRSS) for twin nucleation and propagation, analogous to Schmid's law for
 563 dislocation slip (Thompson and Millard, 1952; Bell and Cahn, 1953; Christian and Mahajan, 1995).
 564 However, experimental results can indicate that twinning dynamics can be more complex (e.g., Bell
 565 and Cahn, 1957). Additional complexities, such as energy barriers for the nucleation of coeval
 566 defects such as stacking faults, disconnections, and unstable transition states associated with
 567 twinning, have also been considered for twinning in metals (e.g., Serra & Bacon; 1996; Kibey et al.,
 568 2007; Pond et al., 2016). Development of a general theory of mechanical twinning applicable to
 569 most minerals is still lacking. Nevertheless, shear modulus G in η_1 along K_1 is highly relevant to
 570 mechanical twinning.

571 Dauphiné twins in α -quartz are merohedral twins, meaning only some atoms exchange their
 572 positions, resulting in a host-twin symmetry relationship that can be described simply by a 180°

573 rotation about the *c*-axis, and recognisable in EBSD maps via a 60° misorientation around the *c*-
 574 axis. The formation of Dauphiné twins has been related to the difference in elastic strain energy
 575 between twinned and un-twinned at constant stress (Thomas & Wooster, 1951; Tullis, 1970; De
 576 Vore, 1970). This difference in elastic strain energy can be written as

$$577 \quad \Delta E = \frac{1}{2} (\sigma_1 - \sigma_3)^2 \Delta s_{11}' \quad (15)$$

578 where $(\sigma_1 - \sigma_3)$ is the applied differential stress, and $\Delta s_{11}' = s_{11}'_{\text{twinned}} - s_{11}'_{\text{un-twinned}}$. Note that s_{11}' is
 579 the reciprocal of the Young's modulus for a given direction. Dauphiné twinning occurs more
 580 readily in those directions for which the strain energy difference (ΔE) is larger, under a boundary
 581 condition of constant axial stress (the inverse is also true: under a condition of constant strain, the
 582 preferred directions of twinning are those that minimise ΔE (Paterson, 1973)). The variation of
 583 $\Delta s_{11}'$ with direction in α -quartz is shown in Figure 18. The stereogram is the same pattern shown in
 584 Thomas & Wooster (1951; their Figure 3a) and Tullis (1970; her Figure 2b). Also shown is a 3D
 585 representation surface of $\Delta s_{11}'$, which emphasises the anisotropy of favoured directions for
 586 Dauphiné twins in α -quartz. The significance of Dauphiné twinning in quartz has recently been
 587 described for sandstones compacted during diagenesis (Mørk and Moen, 2007), deformed in fault
 588 damage zones (Olierook et al., 2014), and deformed by meteorite impact (Wenk et al., 2011; Timms
 589 et al., 2019; Cox et al., 2019), and granitoid protomylonites (Menegon et al., 2011). In all cases,
 590 Dauphiné twins can be used to infer palaeostresses from deformed microstructures. In addition,
 591 Menegon et al. (2011) make the point that Dauphiné twins, formed early in a deformation history,
 592 may effectively store strain energy which is then consumed in later plastic deformation
 593 mechanisms. De Vore (1970) plotted the directional variation of compliances for quartz, ortho- and
 594 clino-pyroxene, hornblende and plagioclase and thereby extended the initial concept of Thomas &
 595 Wooster (1951). To our knowledge, detailed analyses of mechanical twins in these phases has not
 596 yet been related to the anisotropy of elastic compliance or the calculated variations in elastic strain
 597 energy for specific applied loads.

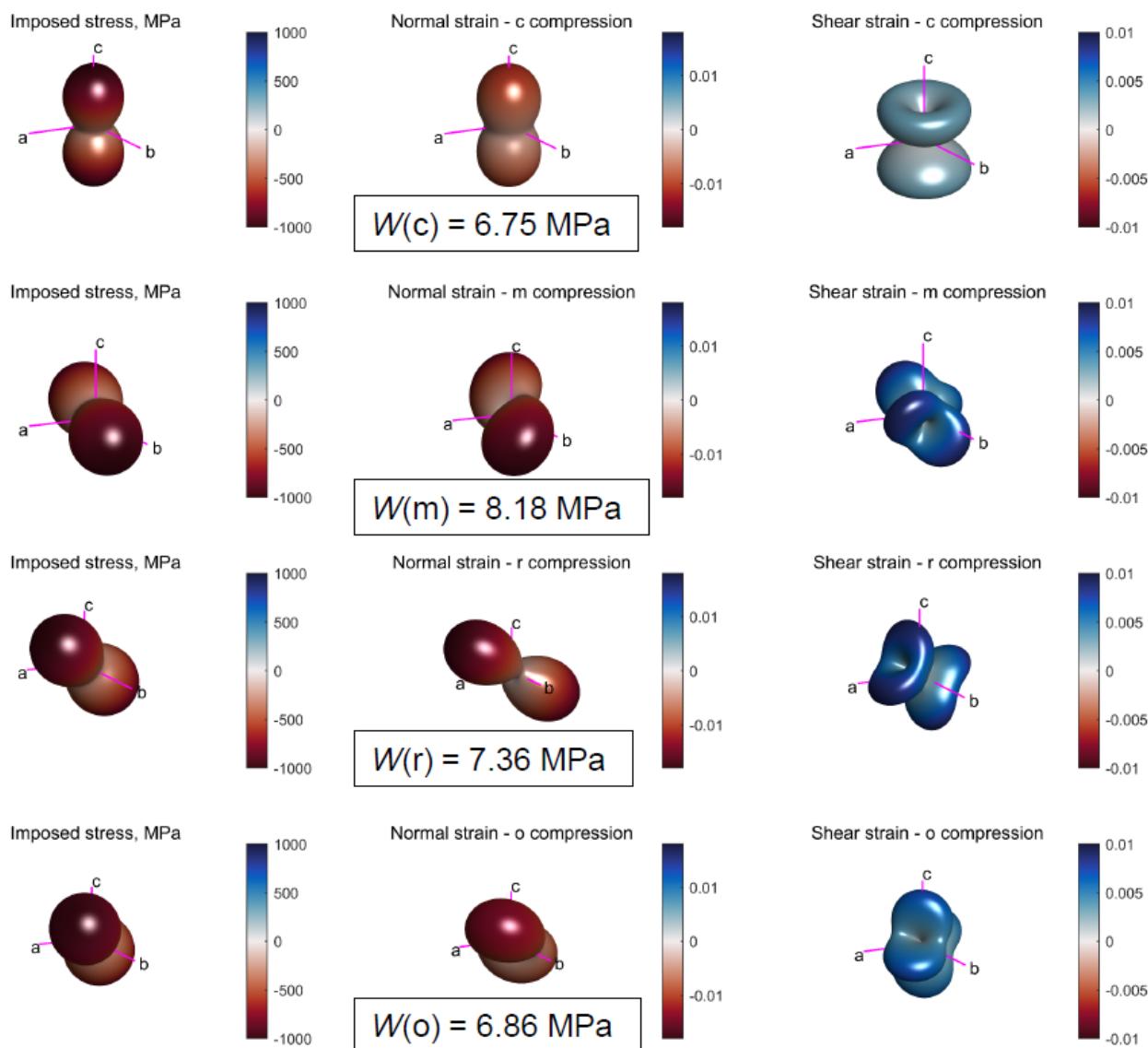


598 **Figure 18.** Anisotropy of $\Delta s_{11}'$ for Dauphiné twinning in α -quartz. $\Delta s_{11}'$ is the difference in the
 599 compliance s_{11}' between the twinned and un-twinned orientations for each direction. **a)** Stereogram
 600 (lower hemisphere, equal area projection) and **b)** a 3D representation surface, both with the
 601 crystallographic reference axes marked. The directions represented by pale yellow/green colours
 602 will be favoured for twinning, whereas the directions shown in blue will not.
 603

604 The relationship between elastic anisotropy and deformation twinning has been investigated in
605 zircon (Timms et al., 2018). In zircon, deformation twins can form as a response to shock
606 conditions and are diagnostic of hypervelocity impact events (Timms et al., 2012; 2017; Erickson et
607 al. 2013). Shock twinning in zircon, which is tetragonal, can occur in up to four symmetrically
608 equivalent orientations, forming along $\{112\}$ composition planes (the of invariant shear, or K_1), and
609 with shear direction $\eta_1 = \langle 111 \rangle$, resulting in a host-twin $65^\circ / \{110\}$ misorientation relationship
610 (Timms et al., 2018). Twinning in this mode has been shown to correspond to the lowest values of
611 G ($G_{\min} = G_{\langle 111 \rangle} = \sim 98$ GPa) (Timms et al., 2018). Furthermore, the lowest values of ν are along
612 $\langle 111 \rangle$ in zircon, indicating that zircon is almost perfectly compressible in $\langle 111 \rangle$ ($\nu_{\min} = \nu_{\langle 111 \rangle} > 0$
613 and $\ll 0.1$) (Timms et al., 2018). These authors illustrate that elastic softness in shear (low G) and a
614 lack of lateral strain in the shear plane ($\nu \sim 0$) are favorable conditions for twinning in zircon
615 (Timms et al. 2018). However, further work is required to determine the critically resolved shear
616 stress for twinning in zircon. Nevertheless, the ability to calculate and visualize anisotropic elastic
617 properties in specific crystallographic directions presented here will be very useful for detailed
618 investigations of mechanical twinning in other phases.

619 *Polymorphic phase transformations*

620 Coherent phase transformations (or transitions) may also be related to the anisotropy of elastic
621 properties, including the α - β transformation in quartz. Coe & Paterson (1969) describe experiments
622 on oriented cores from single crystals of quartz heated to temperatures above the transformation
623 temperature (573°C , at atmospheric pressure), and subjected to non-hydrostatic stress. They found
624 that the temperature of transition was raised by different amounts depending on the orientation of
625 the stress with respect to the crystal. Crystal cores stressed parallel to the c -axis showed the least
626 change, whereas those loaded in the m -direction (perpendicular to c) showed the greatest increase
627 (they also performed experiments on samples cored in the o and r' directions). The temperature of
628 phase transformation from α - (trigonal) to β - (hexagonal) quartz is therefore stress dependent. The
629 theoretical analysis of Coe & Paterson (1969, their Appendix C) ascribes this dependence to an
630 infinitesimal reversible transformation strain, based on the formalism of Eshelby (1957, 1959).
631 Noting that the transformation is also marked by a '*dramatic increase in the development of small-*
632 *scale Dauphine twins*', we have calculated the elastic strain energy per unit volume for each of the
633 four core orientations tested by Coe & Paterson, using their values of applied stress ($\sigma_1 = -1$ GPa,
634 $\sigma_2 = \sigma_3 = -300$ MPa; negative stress compressive) and the elastic constants of α -quartz at 500°C
635 (Lakshtanov et al., 2007). The results are shown in Figure 19, and clearly show an exact correlation
636 with experimental data: the sample loaded in the m direction has the highest strain energy, and that
637 in the c direction has the lowest. The overall sequence is $W(m) > W(r') > W(o) > W(c)$, which
638 precisely mirrors that of the variation in $\partial T / \partial \sigma$ listed for each direction in Coe & Paterson (1969,
639 their Table 3). Therefore, we speculate that the mechanism of phase transformation of α - to β -
640 quartz is probably *not* related to that of Dauphiné twinning in α -quartz, as the temperature
641 difference *increases* for those directions that maximise the elastic strain energy under a constant
642 applied stress. We also note that similar phenomena may occur in pyroxenes (Coe, 1970; Coe &
643 Muller, 1973; Clement et al., 2018).



644
 645 **Figure 19.** Variation in strain (normal and shear) and elastic strain energy for different applied
 646 loads in α -quartz at 500 °C (Lakshtanov et al., 2007). The same compressive stress ($\sigma_1 = -1000$
 647 MPa, $\sigma_2 = \sigma_3 = -300$ MPa) is applied along the *c* (row 1), *m* (row 2), *r* (row 3), and *o* (row 4)
 648 directions in a single crystal. The Reynolds (2nd column) and HWY (3rd column) glyphs show the
 649 normal and shear strains, respectively. The elastic strain energy per unit volume (*W*) is shown for
 650 each configuration. Note that $W(m) > W(r) > W(o) > W(c)$.

651 Visualisation of elastic anisotropy has been used to gain new insights into the effects of intrinsic
 652 elastic stiffness on the transformation from zircon to the high pressure $ZrSiO_4$ polymorph reidite
 653 (Timms et al., 2018). The occurrence of lamellar reidite in shocked zircon from hypervelocity
 654 impact structures has been observed to be spatially limited to low-*U* domains that have not
 655 accumulated radiation damage of the lattice from the decay of U to Pb – a process known as
 656 metamictization (Cavosie et al., 2015; Erickson et al., 2017). Using elastic constants measured for
 657 variably metamict zircon (Özkan, 1976; Özkan and Jamieson, 1978), Timms et al. (2018) illustrated
 658 that the process of metamictization significantly reduces maxima of *E*, *G* and ν in zircon resulting
 659 in a more compliant, isotropic structure. These authors argued that metamict domains in zircon
 660 grains are not elastically stiff enough to support sufficiently high stresses and pressures to facilitate
 661 the transformation to reidite, limiting reidite lamellae to highly crystalline non-metamict domains

662 during the same shock event. This finding illustrates the dependence of elastic properties on lattice
663 defects and a potential role of intrinsic elastic properties in phase transformations.

664 *Metamorphic reactions and equilibrium thermodynamics*

665 The role of elastic deformation in the thermodynamics of preferred orientations and reactions at the
666 scale of individual grains has long been controversial (Macdonald, 1960; Brace, 1960; Kamb, 1961
667 and discussion thereof; Paterson, 1973; Wheeler, 2017). Debate has centred on the role, if any, of
668 the elastic strain energy, W. Macdonald (1960) and Brace (1960) defined the Gibbs free energy of
669 non-hydrostatically stressed minerals in terms of the elastic strain energy, and thereby implicitly
670 defined equilibrium under these conditions. They went on to assert that preferred orientations would
671 develop by the (re-)orientation of a crystals in a given stress system such that their elastic strain
672 energies were maximised. Wheeler (2017), following Kamb (1961) and Paterson (1973), asserts
673 that there is no definable equilibrium in non-hydrostatically stressed systems. Therefore, it is wrong
674 to equate the Gibbs energy for stressed systems of polycrystals to the elastic strain energy.
675 Moreover, the contribution of the elastic strain energy to the chemical potentials along stressed
676 interfaces, through the Helmholtz free energy term, is second order and therefore negligible
677 (Wheeler, 2018).

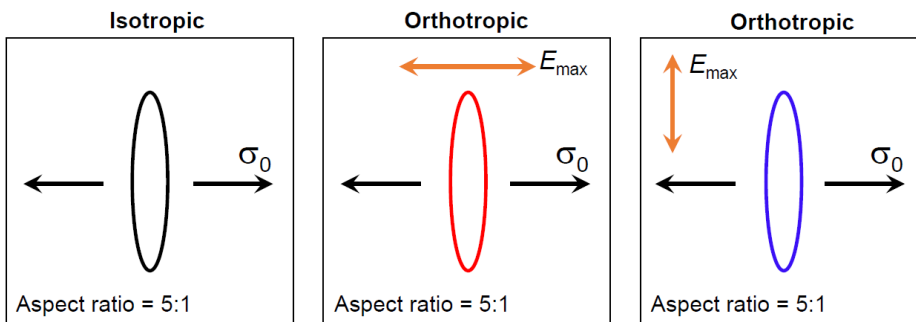
678 *Brittle cracking, decrepitation and dehydration*

679 The magnitude of stresses around fluid-filled pores and cracks developed within single crystalline
680 grains under load can be important for a variety of natural processes. The decrepitation of fluid
681 inclusions occurs when the stresses around the pore exceed the local tensile strength, and the fluid
682 will then drain away. Previous analyses have been rooted in linear elastic fracture mechanics, under
683 an assumption of elastic isotropy. Similarly, in reacting systems the dehydration of hydrous phases
684 can lead to pore fluid overpressures which crack the reacting grain and produce dehydration
685 embrittlement (e.g. Raleigh & Paterson, 1965; Jung et al., 2004). Accurate predictions of the stress
686 levels sustainable by intracrystalline pores and cracks are therefore vital to understanding these
687 fundamental mechanisms. Jaeger & Cook (1969; and repeated by Pollard & Fletcher (2005))
688 asserted that the elastic anisotropy of rocks, measured as the ratio of Young's moduli E_{\max}/E_{\min} , is
689 rarely as high as 2, and therefore the effects of elastic anisotropy are minor to negligible. Davis et
690 al. (2017) used 3D boundary element models to show that Poisson's ratio and void (pore or crack)
691 shape can exert significant control on the local stresses at the void-matrix boundary as a precursor
692 to tensile or shear failure.

693 We have calculated the circumferential stresses around crack-like voids developed within single
694 elastically anisotropic grains of selected minerals (Figures 20 & 21). The model configuration
695 follows that of Jaeger & Cook (1969; derived from Green & Taylor, 1939), and is based on a thin
696 2D orthotropic plate with a single crack of aspect ratio 5:1. The assumption of orthotropy reduces
697 the required elastic constants to five ($E_1, E_2, G, \nu_{21}, \nu_{12}$). We calculated the appropriate values of E ,
698 G and ν from polar plots of anisotropy for the [010] crystallographic plane in each mineral using
699 AnisoVis (see Figure 4d, 5d, 5e-f). For an applied uniaxial tensile load (σ_0 in Figure 20) and a plane
700 strain assumption, the resulting anisotropy of circumferential stress ($\sigma_{\theta\theta}$) at the void-matrix
701 boundary is shown for four different minerals in Figure 21. Each polar plot shows the $\sigma_{\theta\theta}$
702 normalised by the applied load σ_0 in the [010] plane, and for two different configurations of the
703 anisotropy with respect to the load: σ_0 parallel to the direction of E_{\max} (red curves), and

704 perpendicular to the direction of E_{\max} (blue curves). For both of the hydrous sheet silicates talc (c1;
 705 Mainprice et al., 2008) and lizardite (Reynard et al., 2007), the stresses display significant
 706 anisotropy (Figure 21a and b), with amplifications of 6-7 times the stress predicted by assuming the
 707 crystal is isotropic (black curves, calculated with VRH averages of E and ν). These stresses are
 708 likely significant for the failure of cracks or narrow fluid-filled pores in dehydrating subducting
 709 slabs (Healy et al., 2009; Ji et al., 2018). For the two feldspar examples, albite (Brown et al., 2016)
 710 and sanidine (Waesermann et al., 2016), the amplification of circumferential stress is also
 711 significant, at 4-5 times the isotropic prediction. Again, these stresses imply that fluid-filled pores in
 712 phenocrysts of these phases may fail sooner than currently predicted under the assumption of elastic
 713 isotropy. The restriction to 2D may appear limiting in these simple illustrative models, but pending
 714 the development and analysis of fully 3D finite or boundary element models of stresses around
 715 voids in elastically anisotropic media, they can provide useful insights into the relative magnitude
 716 of local stresses and brittle failure. Moreover, we refute the suggestion from Jaeger & Cook (1969)
 717 that as the anisotropy of Young's modulus in rocks is low, the anisotropy of stresses around pores
 718 and cracks is therefore unimportant.

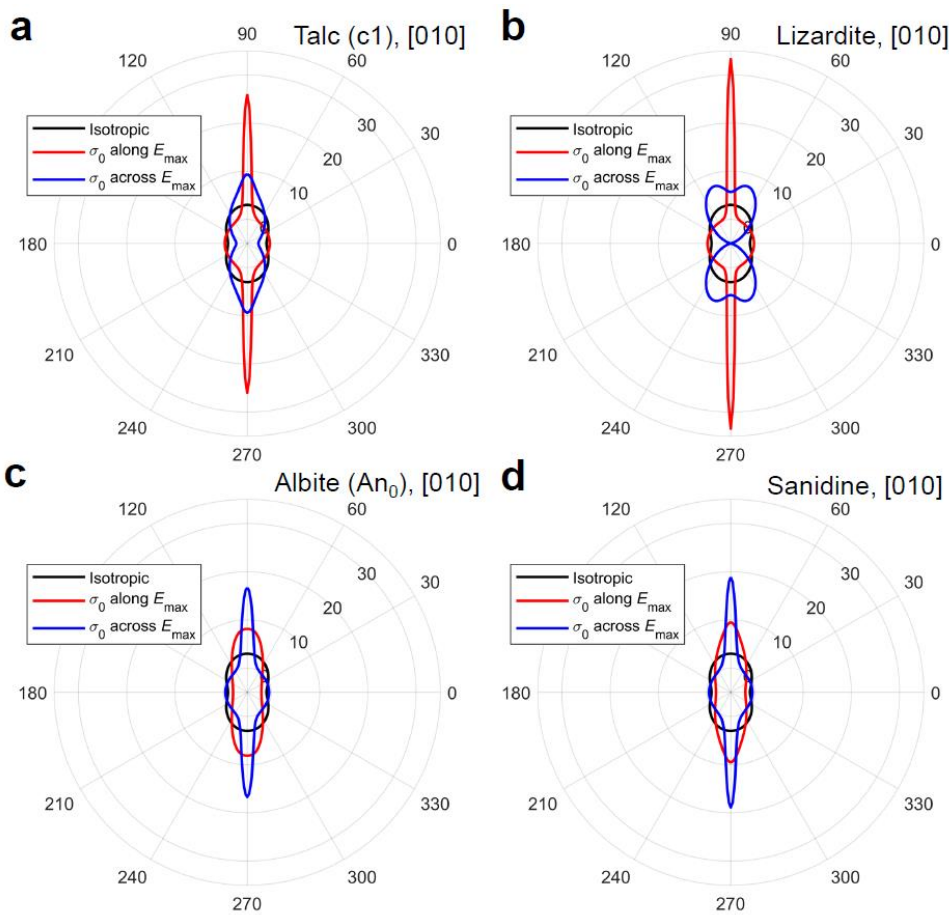
719



720

721 **Figure 20.** Schematic outline for models of narrow cracks in thin 2D orthotropic plates. The crack
 722 is subjected to a uniaxial tensile stress, and plane strain is assumed. The colours of the crack
 723 outlines correspond to the circumferential stress predictions in Figure 21.

724



725

726 **Figure 21.** Predictions of stresses around cracks in thin 2D orthotropic plates. Curves show the
 727 directional variations in the circumferential stress ($\sigma_{\theta\theta}$) normalised by the applied uniaxial tensile
 728 load (σ_0). **a)** Talc (c1, triclinic), (010) plane. **b)** Lizardite, (010) plane. **c)** Albite, (010). **d)**
 729 Sanidine, (010).

730

731 6. Summary

732 We reiterate a key point made by Marmier et al. (2010) in their analysis of chemical compounds:
 733 it's only by visualising elastic anisotropies, preferably in 3D, that we can truly perceive them and
 734 quantify their directions; this then allows us to relate these elastic properties to the underlying
 735 crystal structure and explore the consequences for their behaviour. In developing AnisoVis and
 736 using it to quantify the anisotropy of a specific mineral, we have presented multiple alternative
 737 visualisations of the directional variation of commonly used elastic properties such as Young's
 738 modulus (E), Poisson's ratio (ν), shear modulus (G) and linear compressibility (β). Used in
 739 combination, these depictions serve to increase our understanding of the relationships between the
 740 anisotropy of elastic properties and the underlying crystal symmetry and structure.

741 For example, we note previously unreported directions in certain minerals with negative Poisson's
 742 ratios and negative linear compressibilities. A potentially important consequence of these findings
 743 is that there must also be specific directions along which these properties – Poisson's ratio and
 744 linear compressibility – are 0. These directions will form surfaces in 3D which represent the
 745 boundary between: a) domains of positive and negative Poisson's ratio (both 'regular' and areal),

746 along which a uniaxially applied load will produce no lateral strain; and b) domains of positive and
747 negative linear compressibility, along which an applied hydrostatic load will produce no shortening
748 or stretching. These surfaces and directions in rock-forming minerals may yet lead to new
749 discoveries in the physical behaviour of natural systems and novel applications in materials science
750 or engineering (e.g. Wu et al., 2015).

751 Considering the results from the database of 246 sets of elastic properties, we observe that:

- 752 • significant elastic anisotropy of rock-forming minerals is much **more common** than previously
753 reported e.g. many minerals – 33 of the 86 we analysed – have auxetic directions, and some are
754 areally auxetic;
- 755 • the elastic anisotropy of rock-forming minerals is **wider** than previously reported, with
756 commonly assumed ‘natural limits’ frequently exceeded e.g. Poisson’s ratio for many minerals
757 is either < 0 or > 0.5 .

758 For specific minerals, we also observe that:

- 759 • elastic anisotropy has consequences for intracrystalline stresses under applied strain (and vice
760 versa); the difference between an assumption of isotropy and using the full elastic anisotropy is
761 often of the order of tens of MPa (even for small strains) – i.e. likely to be significant for the
762 deformation around voids such as pores and cracks, especially in dehydrating or decrepitating
763 systems;
- 764 • elastic anisotropy is important for mechanical (deformation) twinning, especially Dauphiné
765 twinning in quartz but probably in other minerals too;
- 766 • coherent phase transformations, such as the α - β transition in quartz, show a clear correlation
767 with the magnitude of elastic strain energy per unit volume and the stress dependence of the
768 transition temperature.

769 *Further work*

770 We are not currently limited by data; we need to process the elasticity data we have and use it to
771 improve our understanding of Earth processes. In theoretical terms, perhaps the biggest advance
772 would come from a solution to the Eshelby problem for an anisotropic inclusion in an anisotropic
773 host, for ellipsoids of general shape and orientation, for the points inside and outside the inclusion.
774 This problem is non-trivial but would be of direct relevance to the inclusion-host studies estimating
775 pressure histories, and for mechanical problems involving voids and cracks in anisotropic crystals,
776 including reacting systems. Numerical modelling studies of the deformation around voids and
777 cracks might usefully incorporate a wider range of values of E and ν . Visualisation of direction-
778 specific elastic properties will be useful for future investigations of the mechanics of twinning,
779 dislocations, and fractures in a wide range of minerals. Earthquake focal mechanisms are known to
780 depend on the elastic anisotropy of the source region (Vavrycuk, 2005), and better understanding of
781 the anisotropies in rock-forming minerals is informing models of fabrics in subducting slabs (Li et
782 al., 2018) and interpretations of microseismicity from commercial hydraulic fracturing operations
783 (Jia et al., 2018). A practical assessment of the contribution of elastic strain energy to metamorphic
784 reactions might involve the systematic mapping of major element chemistry around specific
785 inclusions.

786 We believe that publicly available and easy-to-use software tools like AnisoVis may be useful in
787 teaching environments to guide understanding of the links between mineral properties (elastic,
788 acoustic, optical) and their underlying symmetry and lattice structure. Following Nye’s original
789 text, other properties such as piezoelectric and thermal conductivities, could also be added and
790 visualised (Tommasi, 2001; Mainprice et al., 2015). Our AnisoVis MATLAB source code and
791 sample elasticity files have been made available in open repositories so that other developers and
792 researchers will optimise and extend the functionality, and that “given enough eyeballs, all bugs are
793 shallow” (Raymond, 1999).

794

795 **Code & Data Availability**

796 AnisoVis, including MATLAB source code, a basic user guide and data files for mineral elasticity
797 from published sources, is freely available on:

- 798 • GitHub (<https://github.com/DaveHealy-Aberdeen/AnisoVis>) and
- 799 • Mathworks FileExchange ([https://uk.mathworks.com/matlabcentral/fileexchange/73177-](https://uk.mathworks.com/matlabcentral/fileexchange/73177-anisovis)
800 [anisovis](https://uk.mathworks.com/matlabcentral/fileexchange/73177-anisovis)).

801

802 **Author Contribution**

803 DH designed the software, and wrote the code to calculate the anisotropic elastic properties. NET
804 contributed most of the section on twinning. MAP contributed to the code, especially the
805 calculation of directional properties in Cartesian and crystallographic reference frames. All authors
806 contributed to the manuscript.

807

808 **Competing Interests**

809 The authors declare that they have no conflict of interest.

810

811 **Acknowledgements**

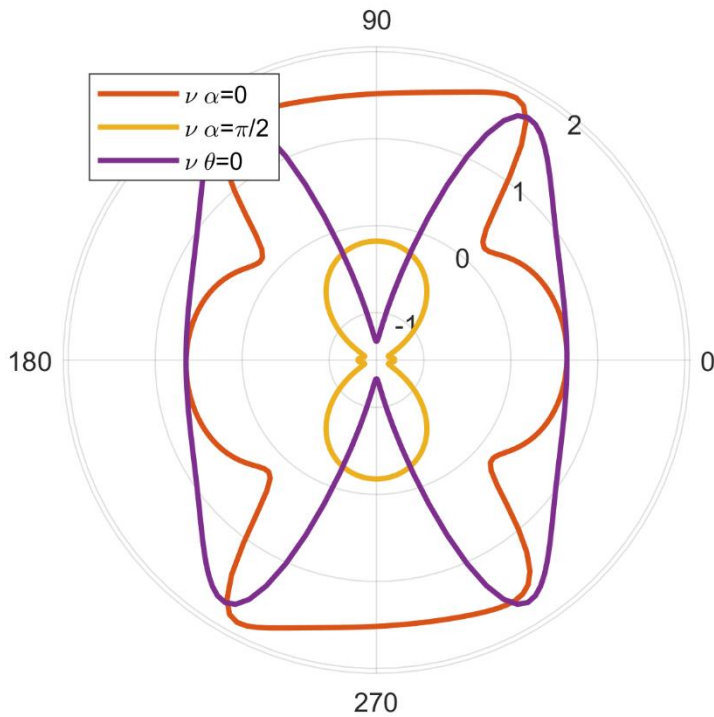
812 DH thanks John Wheeler (Liverpool) for discussion, and Ross Angel (Padua) for discussion and a
813 reprint. This paper is dedicated to the memory of John Frederick Nye (1923-2019) whose seminal
814 text book, first published in 1957 (Physical Properties of Crystals: Their Representation by Tensors
815 and Matrices; reprinted as Nye, 1985), has been a huge influence on the lead author. DH
816 acknowledges financial support from NERC (UK), grant NE/N003063/1.

817

818 **Appendix A – benchmarks to previously published anisotropic elastic properties**

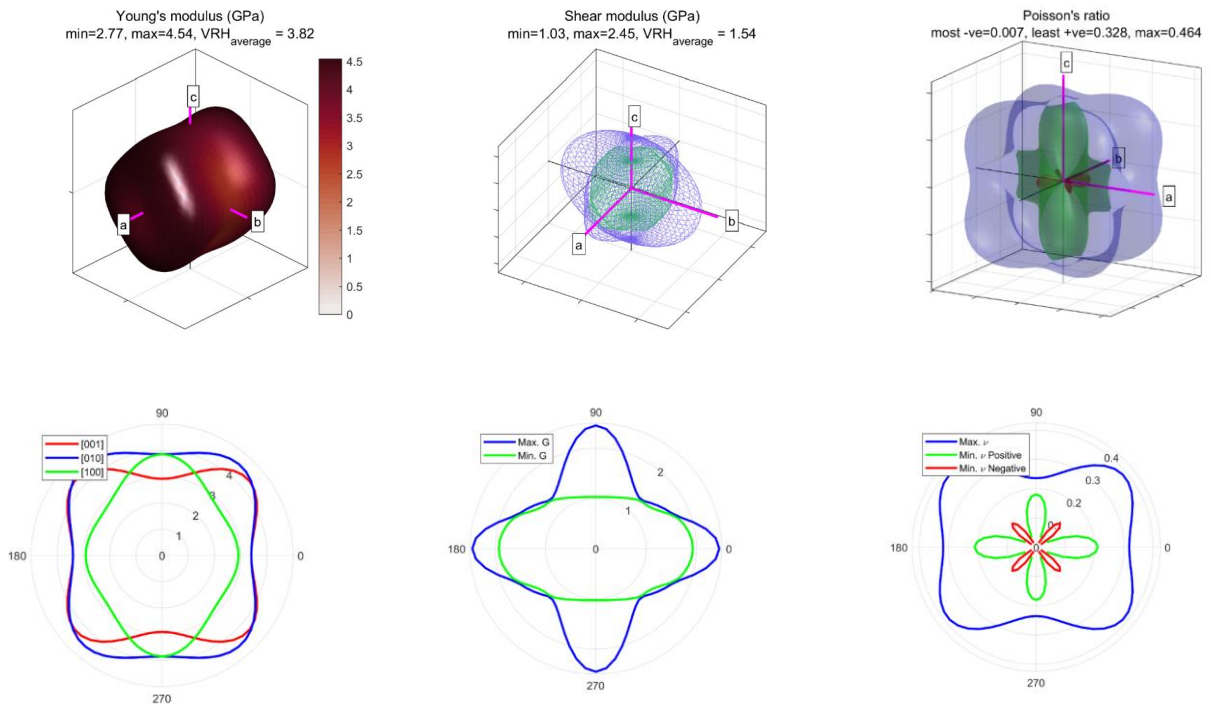
819 The outputs from AnisoVis, and the calculations underlying them, have been benchmarked against
820 previously published examples, chiefly from chemistry and materials science literature. Figures

821 produced by AnisoVis are shown below, with one example per symmetry group, formatted to
 822 mimic the plots in the original publication.

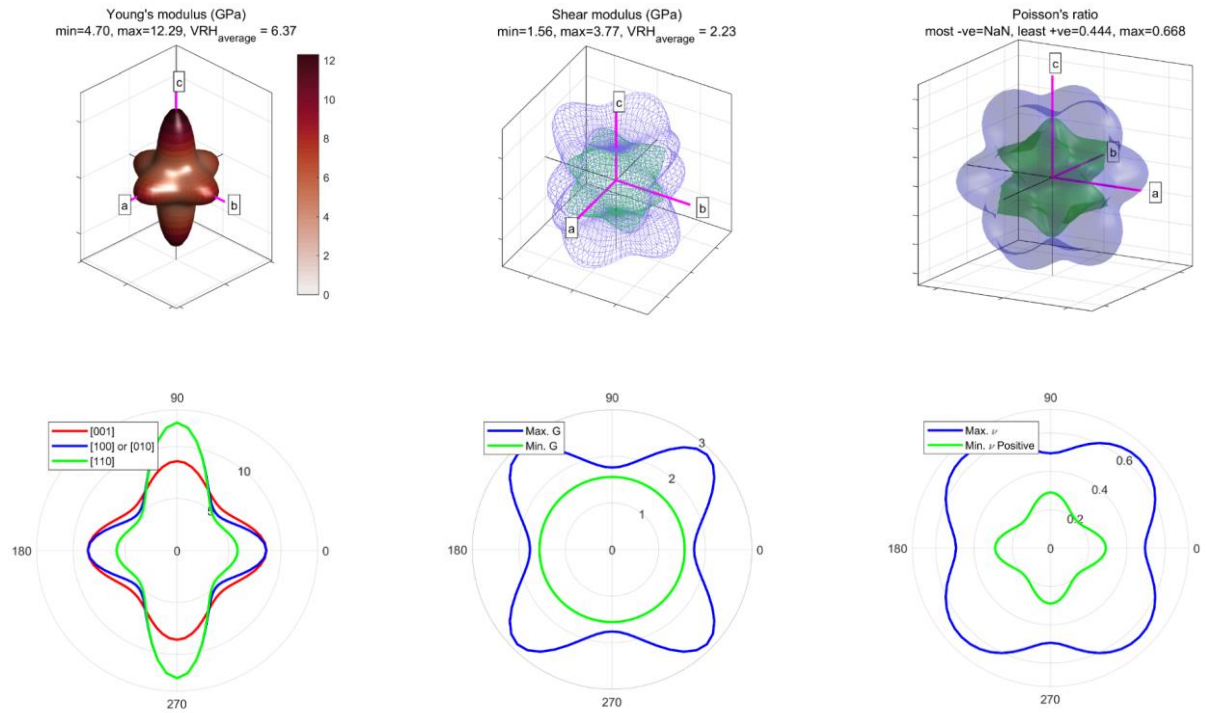


823
 824 **Figure A1.** Benchmarks to Rovati (2004, their Figure 4) for monoclinic cesium dihydrogen
 825 phosphate. Note the extreme auxeticity (negative Poisson's ratio) shown by this material.

826

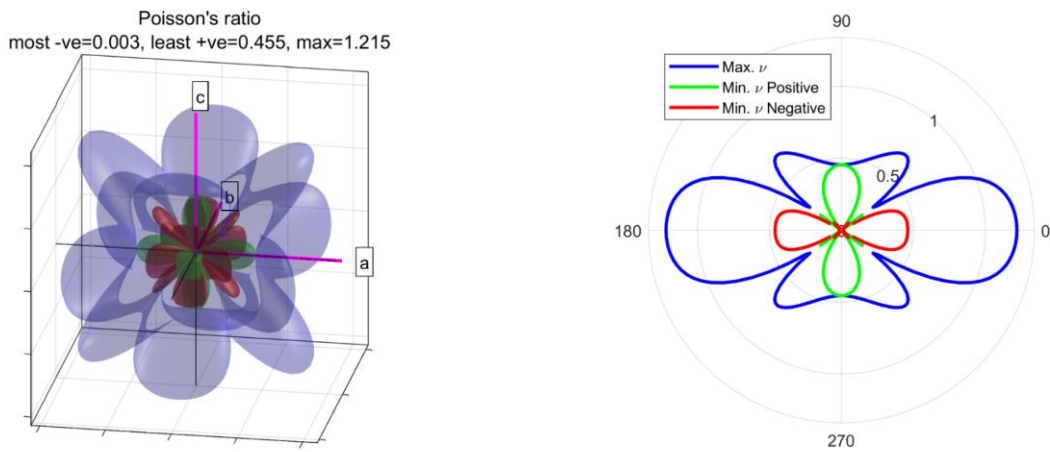


827 **Figure A2.** Benchmarks to Tan et al. (2015, their Figures 2, 3 and 4) for orthorhombic ZIF-4, a
 828 zeolite. Plots shown for Young's modulus, shear modulus and Poisson's ratio.



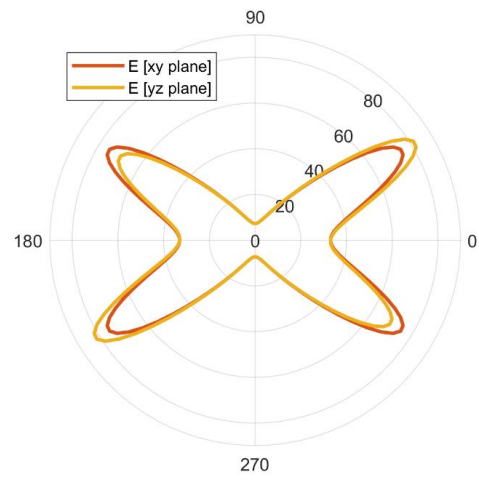
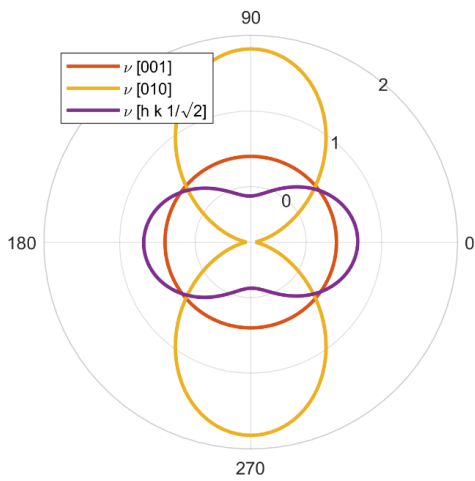
830 **Figure A3.** Benchmarks to Tan et al. (2015, their Figures 2, 3 and 4) for tetragonal ZIF-zni, a
 831 zeolite. Plots shown for Young's modulus, shear modulus and Poisson's ratio.

832



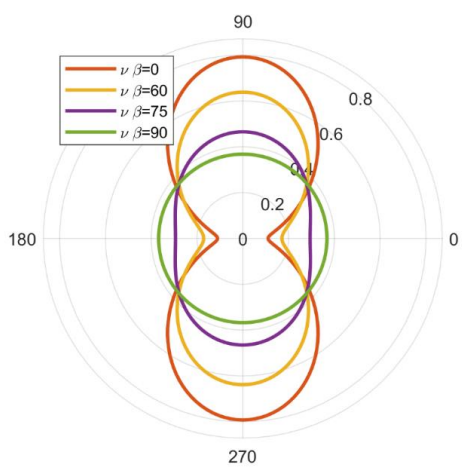
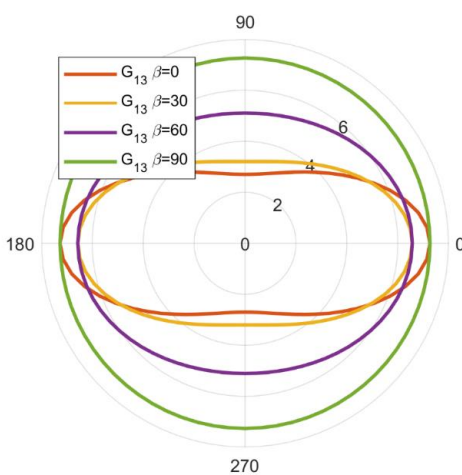
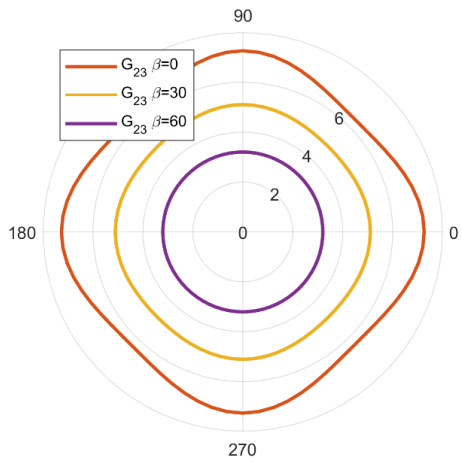
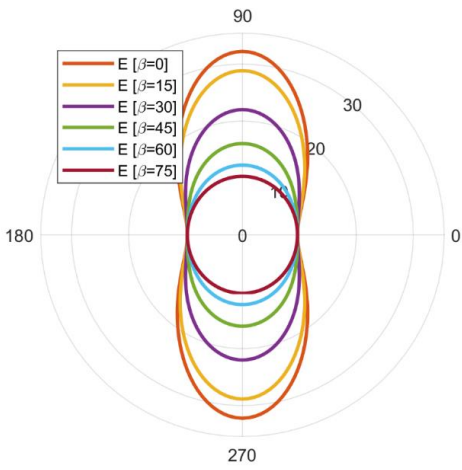
833 **Figure A4.** Benchmarks to Marmier et al. (2010, their Figure 5 and 6) for cubic cesium. Note the
 834 auxetic nature of Poisson's ratio.

835

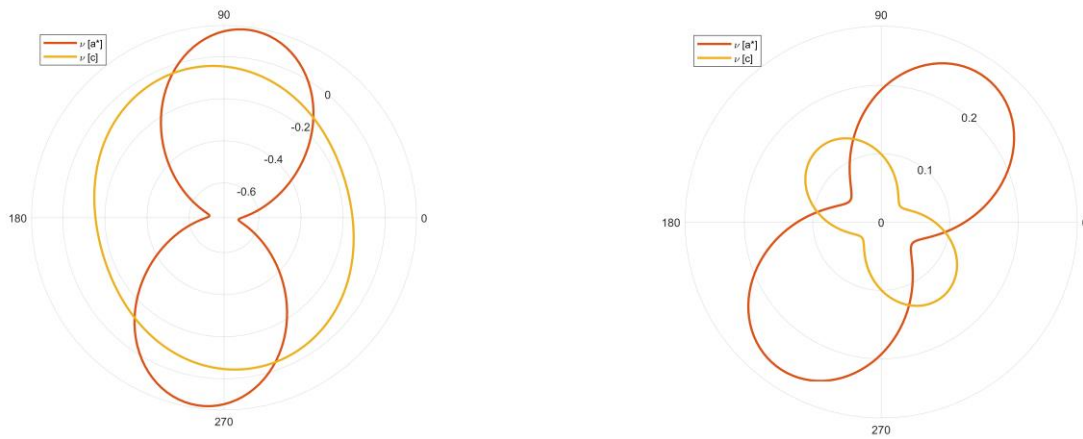


836 **Figure A5.** Benchmarks to Gunton & Saunders (1972, their Figures 3 and 6) for trigonal arsenic.

837



838 **Figure A6.** Benchmarks to Li (1976, their Figure 3) for hexagonal thallium.



839 **Figure A7.** Benchmarks to Mainprice et al. (2008, their Figure 5) for triclinic talc (c1) at 0.0 GPa
 840 (left) and 3.9 GPa (right). The lower pressure example shows auxetic behaviour.

841

842 **References**

843 Aleksandrov, K.S., Ryzhova, T.V. & Belikov, B.P.: The elastic properties of pyroxenes. Soviet
 844 Physics Crystallography, 8, pp.589-591, 1964.

845 Almqvist, B.S. & Mainprice, D.: Seismic properties and anisotropy of the continental crust:
 846 predictions based on mineral texture and rock microstructure. Reviews of Geophysics, 55(2),
 847 pp.367-433, 2017.

848 Anderson, O.L. & Isaak, D.G.: Elastic constants of mantle minerals at high temperature. Mineral
 849 physics and crystallography: a handbook of physical constants, 2, pp.64-97, 1995.

850 Angel, R.J., Sochalski-Kolbus, L.M. and Tribaudino, M. Tilts and tetrahedra: The origin of the
 851 anisotropy of feldspars. *American Mineralogist*, 97(5-6), pp.765-778, 2012.

852 Angel, R.J., Mazzucchelli, M.L., Alvaro, M., Nimis, P. & Nestola, F.: Geobarometry from host-
 853 inclusion systems: the role of elastic relaxation. *American Mineralogist*, 99(10), pp.2146-2149,
 854 2014.

855 Angel, R.J., Nimis, P., Mazzucchelli, M.L., Alvaro, M. & Nestola, F.: How large are departures
 856 from lithostatic pressure? Constraints from host-inclusion elasticity. *Journal of Metamorphic
 857 Geology*, 33(8), pp.801-813, 2015.

858 Aouni, N. & Wheeler, L.: Auxeticity of Calcite and Aragonite polymorphs of CaCO₃ and crystals
 859 of similar structure. *physica status solidi (b)*, 245(11), pp.2454-2462, 2008.

860 Babuska, V. & Cara, M.: Seismic anisotropy in the Earth (Vol. 10). Springer Science & Business
 861 Media, 1991.

862 Bass, J.D.: Elastic properties of minerals, melts, and glasses. *Handbook of Physical Constants*,
 863 pp.45-63, 1995.

- 864 Baughman, R.H., Shacklette, J.M., Zakhidov, A.A. & Stafström, S.: Negative Poisson's ratios as a
865 common feature of cubic metals. *Nature*, 392(6674), p.362, 1998a.
- 866 Baughman, R.H., Stafström, S., Cui, C. & Dantas, S.O.: Materials with negative compressibilities
867 in one or more dimensions. *Science*, 279(5356), pp.1522-1524, 1998b.
- 868 Bell, R. L., & Cahn, R. W.: The nucleation problem in deformation twinning. *Acta Metallurgica*,
869 1(6), 752-753, 1953.
- 870 Bell, R. L., & Cahn, R. W.: The dynamics of twinning and the interrelation of slip and twinning in
871 zinc crystals. *Proceedings of the Royal Society of London. Series A. Mathematical and Physical*
872 *Sciences*, 239(1219), 494-521, 1957.
- 873 Bezacier, L., Reynard, B., Bass, J.D., Sanchez-Valle, C. & Van de Moortèle, B.: Elasticity of
874 antigorite, seismic detection of serpentinites, and anisotropy in subduction zones. *Earth and*
875 *Planetary Science Letters*, 289(1-2), pp.198-208, 2010.
- 876 Birch, A.F. & Bancroft, D.: The elasticity of certain rocks and massive minerals. *American Journal*
877 *of Science*, 237(1), pp.2-6, 1938.
- 878 Brace, W.F.: Orientation of anisotropic minerals in a stress field: discussion. *Geological Society of*
879 *America Memoirs*, 79, pp.9-20, 1960.
- 880 Britton, T.B., Jiang, J., Guo, Y., Vilalta-Clemente, A., Wallis, D., Hansen, L.N., Winkelmann, A. &
881 Wilkinson, A.J.: Tutorial: Crystal orientations and EBSD—Or which way is up?. *Materials*
882 *Characterization*, 117, pp.113-126, 2016.
- 883 Brown, J.M., Angel, R.J. & Ross, N.L.: Elasticity of plagioclase feldspars. *Journal of Geophysical*
884 *Research: Solid Earth*, 121(2), pp.663-675, 2016.
- 885 Cavosie, A. J., Erickson, T. M., & Timms, N. E.: Nanoscale records of ancient shock deformation:
886 Reidite (ZrSiO₄) in sandstone at the Ordovician Rock Elm impact crater. *Geology*, 43(4), 315-318,
887 2015.
- 888 Chen, C.C., Lin, C.C., Liu, L.G., Sinogeikin, S.V. & Bass, J.D.: Elasticity of single-crystal calcite
889 and rhodochrosite by Brillouin spectroscopy. *American Mineralogist*, 86(11-12), pp.1525-1529,
890 2001.
- 891 Chopin, C.: Coesite and pure pyrope in high-grade blueschists of the Western Alps: a first record
892 and some consequences. *Contributions to Mineralogy and Petrology*, 86(2), pp.107-118, 1984.
- 893 Christian, J. W. & Mahajan, S.: Deformation twinning, *Progress in Materials Science*, 39, 1–57,
894 1995.
- 895 Christoffel, E.B.: Über die Fortpflanzung von Stößen durch elastische feste Körper. *Annali di*
896 *Matematica Pura ed Applicata* (1867-1897), 8(1), pp.193-243, 1877.
- 897 Clément, M., Padrón-Navarta, J.A., Tommasi, A. & Mainprice, D.: Non-hydrostatic stress field
898 orientation inferred from orthopyroxene (Pbca) to low-clinoenstatite (P 21/c) inversion in partially
899 dehydrated serpentinites. *American Mineralogist: Journal of Earth and Planetary Materials*, 103(6),
900 pp.993-1001, 2018.

- 901 Coe, R.S.: The thermodynamic effect of shear stress on the ortho-clino inversion in enstatite and
902 other coherent phase transitions characterized by a finite simple shear. *Contributions to mineralogy
903 and petrology*, 26(3), pp.247-264, 1970.
- 904 Coe, R.S. & Paterson, M.S.: The α - β inversion in quartz: a coherent phase transition under
905 nonhydrostatic stress. *Journal of Geophysical Research*, 74(20), pp.4921-4948, 1969.
- 906 Coe, R.S. & Muller, W.F.: Crystallographic orientation of clinoenstatite produced by deformation
907 of orthoenstatite. *Science*, 180(4081), pp.64-66, 1973.
- 908 Cox, M.A., Cavosie, A.J., Ferrière, L., Timms, N.E., Bland, P.A., Miljković, K., Erickson, T.M. &
909 Hess, B.: Shocked quartz in polymict impact breccia from the Upper Cretaceous Yallalie impact
910 structure in Western Australia. *Meteoritics & Planetary Science*, 54(3), pp.621-637, 2019.
- 911 Davis, T., Healy, D., Bubeck, A. & Walker, R.: Stress concentrations around voids in three
912 dimensions: The roots of failure. *Journal of Structural Geology*, 102, pp.193-207, 2017.
- 913 Deer, W., Howie, R. & Zussman, J.: *An introduction to the rock-forming minerals*. Essex. England:
914 Longman Scientific and Technology, 1992.
- 915 DeVore, G.W.: Elastic compliances of minerals related to crystallographic orientation and elastic
916 strain energy relations in twinned crystals. *Lithos*, 3(3), pp.193-208, 1970.
- 917 Erickson, T. M., Cavosie, A. J., Moser, D. E., Barker, I. R. & Radovan, H. A.: Correlating planar
918 microstructures in shocked zircon from the Vredefort Dome at multiple scales: Crystallographic
919 modeling, external and internal imaging, and EBSD structural analysis, *American Mineralogist*, 98,
920 53–65, 2013a.
- 921 Erickson, T. M., Pearce, M. A., Reddy, S. M., Timms, N. E., Cavosie, A. J., Bourdet, J. &
922 Nemchin, A. A.: Microstructural constraints on the mechanisms of the transformation to reidite in
923 naturally shocked zircon. *Contributions to Mineralogy and Petrology*, 172(1), 6, 2017.
- 924 Eshelby, J.D.: The determination of the elastic field of an ellipsoidal inclusion, and related
925 problems. *Proceedings of the Royal Society of London. Series A. Mathematical and Physical
926 Sciences*, 241(1226), pp.376-396, 1957.
- 927 Eshelby, J.D.: The elastic field outside an ellipsoidal inclusion. *Proceedings of the Royal Society of
928 London. Series A. Mathematical and Physical Sciences*, 252(1271), pp.561-569, 1959.
- 929 Gaillac, R., Pullumbi, P. & Coudert, F.X.: ELATE: an open-source online application for analysis
930 and visualization of elastic tensors. *Journal of Physics: Condensed Matter*, 28(27), p.275201, 2016.
- 931 Gercek, H.: Poisson's ratio values for rocks. *International Journal of Rock Mechanics and Mining
932 Sciences*, 44(1), pp.1-13, 2007.
- 933 Gillet, P., Ingrin, J. & Chopin, C.: Coesite in subducted continental crust: PT history deduced from
934 an elastic model. *Earth and Planetary Science Letters*, 70(2), pp.426-436, 1984.
- 935 Greaves, G.N., Greer, A.L., Lakes, R.S. & Rouxel, T.: Poisson's ratio and modern materials. *Nature
936 materials*, 10(11), p.823, 2011.

- 937 Green, A.E. & Taylor, G.I.: Stress systems in aeolotropic plates. I. Proceedings of the Royal Society
938 of London. Series A. Mathematical and Physical Sciences, 173(953), pp.162-172, 1939.
- 939 Gunton, D.J. & Saunders, G.A.: The Young's modulus and Poisson's ratio of arsenic, antimony and
940 bismuth. Journal of Materials Science, 7(9), pp.1061-1068, 1972.
- 941 Guo, C.Y. & Wheeler, L.: Extreme Poisson's ratios and related elastic crystal properties. Journal of
942 the Mechanics and Physics of Solids, 54(4), pp.690-707, 2006.
- 943 Hashash, Y.M., Yao, J.I.C. & Wotring, D.C.: Glyph and hyperstreamline representation of stress
944 and strain tensors and material constitutive response. International journal for numerical and
945 analytical methods in geomechanics, 27(7), pp.603-626, 2003.
- 946 Healy, D., Reddy, S.M., Timms, N.E., Gray, E.M. & Brovarone, A.V.: Trench-parallel fast axes of
947 seismic anisotropy due to fluid-filled cracks in subducting slabs. Earth and Planetary Science
948 Letters, 283(1-4), pp.75-86, 2009.
- 949 Hearmon, R.F.S.: The elastic constants of anisotropic materials. Reviews of Modern Physics, 18(3),
950 p.409, 1946.
- 951 Hearmon, R.F.S.: The third-and higher-order elastic constants. Numerical Data and Functional
952 Relationships in Science and Technology, Landolt-Bornstein, 11, 1979.
- 953 Hearmon, R.F.S.: The elastic constants of crystals and other anisotropic materials. Landolt-
954 Bornstein Tables, III/18, p.1154, 1984.
- 955 Hielscher, R. & Schaeben, H.: A novel pole figure inversion method: specification of the MTEX
956 algorithm. Journal of Applied Crystallography, 41(6), pp.1024-1037, 2008.
- 957 Hill, R.: The elastic behaviour of a crystalline aggregate. Proceedings of the Physical Society.
958 Section A, 65(5), p.349, 1952.
- 959 Jaeger, J.C. & Cook, N.G.: *Fundamentals of rock mechanics*. Methuen & Co. Ltd., London, 513,
960 1969.
- 961 Ji, S., Li, L., Motra, H.B., Wuttke, F., Sun, S., Michibayashi, K. & Salisbury, M.H.: Poisson's ratio
962 and auxetic properties of natural rocks. Journal of Geophysical Research: Solid Earth, 123(2),
963 pp.1161-1185, 2018.
- 964 Jia, S.Q., Eaton, D.W. & Wong, R.C.: Stress inversion of shear-tensile focal mechanisms with
965 application to hydraulic fracture monitoring. Geophysical Journal International, 215(1), pp.546-563,
966 2018.
- 967 Jung, H., Green II, H.W. & Dobrzhinetskaya, L.F.: Intermediate-depth earthquake faulting by
968 dehydration embrittlement with negative volume change. Nature, 428(6982), p.545, 2004.
- 969 Kamb, W.B.: The thermodynamic theory of nonhydrostatically stressed solids. Journal of
970 Geophysical Research, 66(1), pp.259-271, 1961.
- 971 Karki, B.B. & Chennamsetty, R.: A visualization system for mineral elasticity. Visual Geosciences,
972 9(1), pp.49-57, 2004.

- 973 Kern, H.: Elastic-wave velocity in crustal and mantle rocks at high pressure and temperature: the
974 role of the high-low quartz transition and of dehydration reactions. *Physics of the Earth and*
975 *Planetary Interiors*, 29(1), pp.12-23, 1982.
- 976 Kibey, S., Liu, J. B., Johnson, D. D. & Sehitoglu, H.: Predicting twinning stress in fcc metals:
977 Linking twin-energy pathways to twin nucleation, *Acta Mater.*, 55, 6843–6851, 2007.
- 978 Kratz, A., Auer, C. & Hotz, I.: *Tensor Invariants and Glyph Design. In Visualization and*
979 *Processing of Tensors and Higher Order Descriptors for Multi-Valued Data* (pp. 17-34). Springer,
980 Berlin, Heidelberg, 2014.
- 981 Lacazette, A.: Application of linear elastic fracture mechanics to the quantitative evaluation of
982 fluid-inclusion decrepitation. *Geology*, 18(8), pp.782-785, 1990.
- 983 Lakes, R.: Foam structures with a negative Poisson's ratio. *Science*, 235, pp.1038-1041, 1987.
- 984 Lakshatanov, D.L., Sinogeikin, S.V. & Bass, J.D.: High-temperature phase transitions and elasticity
985 of silica polymorphs. *Physics and Chemistry of Minerals*, 34(1), pp.11-22, 2007.
- 986 Lethbridge, Z.A., Walton, R.I., Marmier, A.S., Smith, C.W. & Evans, K.E.: Elastic anisotropy and
987 extreme Poisson's ratios in single crystals. *Acta Materialia*, 58(19), pp.6444-6451, 2010.
- 988 Li, Y.: The anisotropic behavior of Poisson's ratio, Young's modulus, and shear modulus in
989 hexagonal materials. *physica status solidi (a)*, 38(1), pp.171-175, 1976.
- 990 Li, J., Zheng, Y., Thomsen, L., Lapen, T.J. & Fang, X.: Deep earthquakes in subducting slabs
991 hosted in highly anisotropic rock fabric. *Nature Geoscience*, 11(9), p.696, 2018.
- 992 Lloyd, G.E. & Kendall, J.M.: Petrofabric-derived seismic properties of a mylonitic quartz simple
993 shear zone: implications for seismic reflection profiling. Geological Society, London, Special
994 Publications, 240(1), pp.75-94, 2005.
- 995 MacDonald, G.J.: Orientation of anisotropic minerals in a stress field. Geological Society of
996 America Memoirs, 79, pp.1-8, 1960.
- 997 Mainprice, D.: A FORTRAN program to calculate seismic anisotropy from the lattice preferred
998 orientation of minerals. *Computers & Geosciences*, 16(3), pp.385-393, 1990.
- 999 Mainprice, D. & Casey, M.: The calculated seismic properties of quartz mylonites with typical
1000 fabrics: relationship to kinematics and temperature. *Geophysical Journal International*, 103(3),
1001 pp.599-608, 1990.
- 1002 Mainprice, D., Le Page, Y., Rodgers, J. & Jouanna, P.: Ab initio elastic properties of talc from 0 to
1003 12 GPa: interpretation of seismic velocities at mantle pressures and prediction of auxetic behaviour
1004 at low pressure. *Earth and Planetary Science Letters*, 274(3-4), pp.327-338, 2008.
- 1005 Mainprice, D., Hielscher, R. & Schaeben, H.: Calculating anisotropic physical properties from
1006 texture data using the MTEX open-source package. Geological Society, London, Special
1007 Publications, 360(1), pp.175-192, 2011.

- 1008 Mainprice, D., Bachmann, F., Hielscher, R., Schaeben, H. & Lloyd, G.E.: Calculating anisotropic
1009 piezoelectric properties from texture data using the MTEX open source package. Geological
1010 Society, London, Special Publications, 409(1), pp.223-249, 2015.
- 1011 Mandell, W.: The determination of the elastic moduli of the piezo-electric crystal Rochelle salt by a
1012 statical method. Proceedings of the Royal Society of London. Series A, Containing Papers of a
1013 Mathematical and Physical Character, 116(775), pp.623-636, 1927.
- 1014 Manghnani, M.H.: Elastic constants of single-crystal rutile under pressures to 7.5 kilobars. Journal
1015 of Geophysical Research, 74(17), pp.4317-4328, 1969.
- 1016 Mao, Z., Jiang, F. & Duffy, T.S.: Single-crystal elasticity of zoisite $\text{Ca}_2\text{Al}_3\text{Si}_3\text{O}_{12}(\text{OH})$ by
1017 Brillouin scattering. American Mineralogist, 92(4), pp.570-576, 2007.
- 1018 Marmier, A., Lethbridge, Z.A., Walton, R.I., Smith, C.W., Parker, S.C. & Evans, K.E.: ElAM: A
1019 computer program for the analysis and representation of anisotropic elastic properties. Computer
1020 Physics Communications, 181(12), pp.2102-2115, 2010.
- 1021 Mazzucchelli, M.L., Burnley, P., Angel, R.J., Morganti, S., Domeneghetti, M.C., Nestola, F. &
1022 Alvaro, M.: Elastic geothermobarometry: Corrections for the geometry of the host-inclusion
1023 system. Geology, 46(3), pp.231-234, 2018.
- 1024 Menegon, L., Piazzolo, S. & Pennacchioni, G.: The effect of Dauphiné twinning on plastic strain in
1025 quartz. Contributions to Mineralogy and Petrology, 161(4), pp.635-652, 2011.
- 1026 Militzer, B., Wenk, H.R., Stackhouse, S. & Stixrude, L.: First-principles calculation of the elastic
1027 moduli of sheet silicates and their application to shale anisotropy. American Mineralogist, 96(1),
1028 pp.125-137, 2011.
- 1029 Moore, J.G., Schorn, S.A. & Moore, J.: Methods of Classical Mechanics Applied to Turbulence
1030 Stresses in a Tip Leakage Vortex. Journal of turbomachinery, 118(4), pp.622-629, 1996.
- 1031 Mörk, M. B. E., & Moen, K.: Compaction microstructures in quartz grains and quartz cement in
1032 deeply buried reservoir sandstones using combined petrography and EBSD analysis. Journal of
1033 Structural Geology, 29(11), 1843-1854, 2007.
- 1034 Nye, J.F.: *Physical properties of crystals: their representation by tensors and matrices*. Oxford
1035 University Press, 1985.
- 1036 Ogi, H., Ohmori, T., Nakamura, N. & Hirao, M.: Elastic, anelastic, and piezoelectric coefficients of
1037 α -quartz determined by resonance ultrasound spectroscopy. Journal of Applied Physics, 100(5),
1038 p.053511, 2006.
- 1039 Olierook, H. K., Timms, N. E., & Hamilton, P. J.: Mechanisms for permeability modification in the
1040 damage zone of a normal fault, northern Perth Basin, Western Australia. Marine and Petroleum
1041 Geology, 50, 130-147, 2014.
- 1042 Özkan, H.: Effect of nuclear radiation on the elastic moduli of zircon. Journal of Applied Physics,
1043 47(11), 4772-4779, 1976.

- 1044 Özkan, H., & Jamieson, J. C.: Pressure dependence of the elastic constants of non-metamict zircon.
1045 *Physics and Chemistry of Minerals*, 2(3), 215-224, 1978.
- 1046 Pabst, W. & Gregorová, E.V.A.: Elastic properties of silica polymorphs—a review. *Ceramics-*
1047 *Silikaty*, 57(3), pp.167-184, 2013.
- 1048 Pasternak, E. & Dyskin, A.V.: Materials and structures with macroscopic negative Poisson's ratio.
1049 *International Journal of Engineering Science*, 52, pp.103-114, 2012.
- 1050 Paterson, M.S.: Nonhydrostatic thermodynamics and its geologic applications. *Reviews of*
1051 *Geophysics*, 11(2), pp.355-389, 1973.
- 1052 Pollard, D.D. & Fletcher, R.C.: *Fundamentals of Structural Geology*. Cambridge University Press,
1053 pp.512, 2005.
- 1054 Pond, R. C., Hirth, J. P., Serra, A., & Bacon, D. J.: Atomic displacements accompanying
1055 deformation twinning: shears and shuffles. *Materials Research Letters*, 4(4), 185-190, 2016.
- 1056 Prawoto, Y.: Seeing auxetic materials from the mechanics point of view: a structural review on the
1057 negative Poisson's ratio. *Computational Materials Science*, 58, pp.140-153, 2012.
- 1058 Raleigh, C.B. & Paterson, M.S.: Experimental deformation of serpentinite and its tectonic
1059 implications. *Journal of Geophysical Research*, 70(16), pp.3965-3985, 1965.
- 1060 Ranganathan, S.I. & Ostoja-Starzewski, M.: Universal elastic anisotropy index. *Physical Review*
1061 *Letters*, 101(5), p.055504, 2008.
- 1062 Raymond, E.: The cathedral and the bazaar. *Knowledge, Technology & Policy*, 12(3), pp.23-49,
1063 1999.
- 1064 Reynard, B., Hilairet, N., Balan, E. & Lazzeri, M.: Elasticity of serpentines and extensive
1065 serpentinization in subduction zones. *Geophysical Research Letters*, 34(13), 2007.
- 1066 Rosenfeld, J.L.: Stress effects around quartz inclusions in almandine and the piezothermometry of
1067 coexisting aluminum silicates. *American Journal of Science*, 267(3), pp.317-351, 1969.
- 1068 Rosenfeld, J.L. & Chase, A.B.: Pressure and temperature of crystallization from elastic effects
1069 around solid inclusions in minerals?. *American Journal of Science*, 259(7), pp.519-541, 1961.
- 1070 Rovati, M.: Directions of auxeticity for monoclinic crystals. *Scripta materialia*, 51(11), pp.1087-
1071 1091, 2004.
- 1072 Rutter, E. H.: Pressure solution in nature, theory and experiment. *Journal of the Geological Society*,
1073 140(5), 725-740, 1983.
- 1074 Ryzhova, T. V.: Elastic properties of plagioclases, *Akad. SSSR Izv. Ser. Geofiz.*, 7, 1049–1051,
1075 1964.
- 1076 Serra, A., & Bacon, D. J.: A new model for {10 1 2} twin growth in hcp metals. *Philosophical*
1077 *Magazine A*, 73(2), 333-343, 1996.
1078

- 1079 Sinogeikin, S.V., Schilling, F.R. & Bass, J.D.: Single crystal elasticity of lawsonite. *American*
1080 *Mineralogist*, 85(11-12), pp.1834-1837, 2000.
- 1081 Tan, J.C., Civalleri, B., Erba, A. & Albanese, E.: Quantum mechanical predictions to elucidate the
1082 anisotropic elastic properties of zeolitic imidazolate frameworks: ZIF-4 vs. ZIF-zni.
1083 *CrystEngComm*, 17(2), pp.375-382, 2015.
- 1084 Tatham, D.J., Lloyd, G.E., Butler, R.W.H. & Casey, M.: Amphibole and lower crustal seismic
1085 properties. *Earth and Planetary Science Letters*, 267(1-2), pp.118-128, 2008.
- 1086 Thomas, L.A. & Wooster, W.A.: Piezoerescence—the growth of Dauphiné twinning in quartz
1087 under stress. *Proceedings of the Royal Society of London. Series A. Mathematical and Physical*
1088 *Sciences*, 208(1092), pp.43-62, 1951.
- 1089 Thyng, K.M., Greene, C.A., Hetland, R.D., Zimmerle, H.M. & DiMarco, S.F.: True colors of
1090 oceanography: Guidelines for effective and accurate colormap selection. *Oceanography*, 29(3),
1091 pp.9-13, 2016.
- 1092 Timms, N.E., Healy, D., Reyes-Montes, J.M., Collins, D.S., Prior, D.J. & Young, R.P.: Effects of
1093 crystallographic anisotropy on fracture development and acoustic emission in quartz. *Journal of*
1094 *Geophysical Research: Solid Earth*, 115(B7), 2010.
- 1095 Timms, N. E., Reddy, S. M., Healy, D., Nemchin, A. A., Grange, M. L., Pidgeon, R. T., & Hart, R.:
1096 Resolution of impact-related microstructures in lunar zircon: A shock-deformation mechanism map.
1097 *Meteoritics & Planetary Science*, 47(1), 120-141, 2012.
- 1098 Timms, N.E., Erickson, T.M., Pearce, M.A., Cavosie, A.J., Schmieder, M., Tohver, E., Reddy,
1099 S.M., Zanetti, M.R., Nemchin, A.A. & Wittmann, A.: A pressure-temperature phase diagram for
1100 zircon at extreme conditions. *Earth-Science Reviews*, 165, pp.185-202, 2017.
- 1101 Timms, N.E., Healy, D., Erickson, T.M., Nemchin, A.A., Pearce, M.A. & Cavosie, A.J.: The role of
1102 elastic anisotropy in the development of deformation microstructures in zircon. In: Moser, D.,
1103 Corfu, F., Reddy, S., Darling, J., Tait, K. (Eds.), *AGU Monograph: Microstructural Geochronology;*
1104 *Lattice to Atom-Scale Records of Planetary Evolution*. AGU-Wiley, 183-202, 2018.
- 1105 Timms, N.E., Pearce, M.A., Erickson, T.M., Cavosie, A.J., Rae, A.S., Wheeler, J., Wittmann, A.,
1106 Ferrière, L., Poelchau, M.H., Tomioka, N. & Collins, G.S.: New shock microstructures in titanite
1107 (CaTiSiO₅) from the peak ring of the Chicxulub impact structure, Mexico. *Contributions to*
1108 *Mineralogy and Petrology*, 174(5), p.38, 2019.
- 1109 Thompson, N., & Millard, D. J.: Twin formation, in cadmium. *The London, Edinburgh, and Dublin*
1110 *Philosophical Magazine and Journal of Science*, 43(339), 422-440, 1952.
- 1111 Ting, T.C.T. & Chen, T.: Poisson's ratio for anisotropic elastic materials can have no bounds. *The*
1112 *quarterly journal of mechanics and applied mathematics*, 58(1), pp.73-82, 2005.
- 1113 Tommasi, A., Gibert, B., Seipold, U. & Mainprice, D.: Anisotropy of thermal diffusivity in the
1114 upper mantle. *Nature*, 411(6839), p.783, 2001.

- 1115 Tomé, C. N., & Lebensohn, R. A.: Manual for Code Visco-Plastic Self-Consistent (VPSC) (Version
1116 7c). Los Alamos National Laboratory, USA, 2009.
- 1117 Tullis, J.: Quartz: preferred orientation in rocks produced by Dauphiné twinning. *Science*,
1118 168(3937), pp.1342-1344, 1970.
- 1119 Turley, J. & Sines, G.: The anisotropy of Young's modulus, shear modulus and Poisson's ratio in
1120 cubic materials. *Journal of Physics D: Applied Physics*, 4(2), p.264, 1971.
- 1121 Van der Molen, I. & Van Roermund, H.L.M.: The pressure path of solid inclusions in minerals: the
1122 retention of coesite inclusions during uplift. *Lithos*, 19(3-4), pp.317-324, 1986.
- 1123 Vavryčuk, V.: Focal mechanisms in anisotropic media. *Geophysical Journal International*, 161(2),
1124 pp.334-346, 2005.
- 1125 Verma, R.K.: Elasticity of some high-density crystals. *Journal of Geophysical Research*, 65(2),
1126 pp.757-766, 1960.
- 1127 Waesermann, N., Brown, J.M., Angel, R.J., Ross, N., Zhao, J. & Kaminsky, W.: The elastic tensor
1128 of monoclinic alkali feldspars. *American Mineralogist*, 101(5), pp.1228-1231, 2016.
- 1129 Walker, A.M. & Wookey, J.: MSAT—A new toolkit for the analysis of elastic and seismic
1130 anisotropy. *Computers & Geosciences*, 49, pp.81-90, 2012.
- 1131 Weidner, D.J. & Carleton, H.R.: Elasticity of coesite. *Journal of Geophysical Research*, 82(8),
1132 pp.1334-1346, 1977.
- 1133 Wenk, H.R., Janssen, C., Kenkmann, T. & Dresen, G.: Mechanical twinning in quartz: shock
1134 experiments, impact, pseudotachylites and fault breccias. *Tectonophysics*, 510(1-2), pp.69-79,
1135 2011.
- 1136 Wheeler, J.: Importance of pressure solution and Coble creep in the deformation of polymineralic
1137 rocks. *Journal of Geophysical Research: Solid Earth*, 97(B4), 4579-4586, 1992.
- 1138 Wheeler, J.: The effects of stress on reactions in the Earth: Sometimes rather mean, usually normal,
1139 always important. *Journal of Metamorphic Geology*, 36(4), pp.439-461, 2018.
- 1140 Wu, Y., Yi, N., Huang, L., Zhang, T., Fang, S., Chang, H., Li, N., Oh, J., Lee, J.A., Kozlov, M. &
1141 Chipara, A.C.: Three-dimensionally bonded spongy graphene material with super compressive
1142 elasticity and near-zero Poisson's ratio. *Nature communications*, 6, p.6141, 2015.
- 1143 Yeganeh-Haeri, A., Weidner, D.J. & Parise, J.B.: Elasticity of α -cristobalite: a silicon dioxide with
1144 a negative Poisson's ratio. *Science*, 257(5070), pp.650-652, 1992.
- 1145 Zhang, Y.: Mechanical and phase equilibria in inclusion–host systems. *Earth and Planetary Science*
1146 *Letters*, 157(3-4), pp.209-222, 1998.
- 1147 Zhou, B. & Greenhalgh, S.: On the computation of elastic wave group velocities for a general
1148 anisotropic medium. *Journal of Geophysics and Engineering*, 1(3), pp.205-215, 2004.
- 1149